A spatial model of the plant circadian clock reveals design principles for coordinated timing under noisy environments

Short title: Coordinated timing through clock coupling

Mark Greenwood[1,2], Isao T. Tokuda[3*], James C.W. Locke[1,4*]

[1]Sainsbury Laboratory, University of Cambridge, Cambridge, UK

[2]Department of Biochemistry, University of Cambridge, Cambridge, UK

[3]Department of Mechanical Engineering, Ritsumeikan University, Kusatsu, Japan

[4]Microsoft Research, Cambridge, UK

[*]For correspondence: james.locke@slcu.cam.ac.uk or isao@fc.ritsumei.ac.jp

Abstract

Individual plant cells possess a genetic network, the circadian clock, that times internal processes to the day-night cycle. Mathematical models of the clock network have driven a mechanistic understanding of the clock in plants. However, these models are typically either 'whole plant' models that ignore tissue or cell type specific clock behavior, or 'phase only' models that do not include clock network components explicitly. It is increasingly clear that clock network models must address spatial differences, as complex spatial behaviors have been observed in tissues and cells in plants, including period and phase differences between cells and spatial waves of gene expression between organs. Here, we implement an up to date clock network model on a spatial template of the plant. In our model, the sensitivity to light inputs varies across the plant, and cells communicate their clock timing locally via the levels of core clock mRNA levels by cell-to-cell coupling. We found that differences in sensitivities to environmental input in the model can explain the experimentally observed differences in clock periods in different organs, and we show using the model that a plausible coupling mechanism

can generate the experimentally observed waves in clock gene expression across the plant. We then examined what features of the plant circadian system allow it to keep time under noisy light-dark (LD) cycles. We found that differences in sensitivity to light can allow regional flexibility in phase even under LD cycles, whilst local cell-to-cell coupling minimized variability in clock rhythms in neighboring cells. Thus, local sensitivity to environmental inputs combined with cell-to-cell coupling allows for flexible yet robust circadian timing under noisy environments.

Abbreviations: *CCA1*, *CIRCADIAN CLOCK ASSOCIATED 1*; CV, coefficient of variation; DD, constant dark; *ELF4*, *EARLY FLOWERING 4*; LD, light-dark; *LHY*, *LATE ELONGATED HYPOCOTYL*; LL, constant light; *LUC*, *LUCIFERASE*; *LUX*, *LUX ARRHYTHMO*; *PRR*, *PSEUDO-RESPONSE REGULATOR*; *TOC1*, *TIMING OF CAB EXPRESSION 1*; YFP, yellow fluorescent protein.

Introduction

The circadian clock is a 24 h genetic oscillator found in many organisms. The clock consists of a circuit of interlocking feedback loops of mRNAs and proteins that generate daily oscillations in circuit component levels. Signals from the environment align the timing of these oscillations to the day-night cycle [1]. Once set, circadian clocks act as an internal timing signal, allowing biological processes to anticipate the external environmental cycles. The circadian clock modulates a diverse range of processes in plants, including cell division, tissue growth, flowering time, and scent emission [2–5]. Altogether this daily timing provides a significant fitness advantage to the plant [6,7].

Individual plant cells possess a robust circadian clock [8]. However, substantial differences in the period and phase of clock rhythms across the plant have been observed. Time lapse imaging experiments with luciferase and fluorescent reporter genes have shown that rhythms in

core clock genes oscillate with different speeds in different organs under constant light (LL) [8–13]. Further, experiments under a range of conditions have shown that differences in clock speed and phase can be caused by organs having different sensitivity to environmental signals [12–15]. Differences in the clock network between tissues may also contribute to generating differences in rhythms across the plant, as although the clock genes are broadly expressed [13], some are tissue enriched [16], and mutations can affect organs differently [11,15,17].

The observed differences in clock rhythms across the plant raises the question of how clocks in different cells and tissues remain coordinated with each other. One mechanism would be for cells to communicate their timing with their neighbors. High resolution experiments have measured or inferred local coupling of clock rhythms between cells [8,11,14,16,18–20], and local coupling can drive spatial waves of clock gene expression across the plant [8,14,18–20]. Longer-distance coupling between clocks is also possible. For example, molecular signals communicate temperature information from the shoot to the root [11,21], and light information may be piped down the stem [22].

Mathematical modelling has played a crucial role in gaining a mechanistic understanding of plant circadian clocks. Models of the network have increased in complexity over time in parallel with the growing number of experiments [23–28]. Recently, these detailed molecular models have been used to probe the differences between the shoot and root clock [13]. However, the coupling of clocks between cells was not considered. For this, more computationally tractable models of the clock network are necessary. Reduced models of the network have already been constructed that capture many of the features of the single cell clock dynamics [29–32]. However, these models have not been applied to study spatial dynamics. Instead, ‘phase only’ models that lack any genetic network information and only consider the phases of individual cellular rhythms, have been preferred [8,18–20]. Although these models allow the simulation of

general oscillatory behavior, owing to their simplicity they are unsuitable for investigating molecular mechanisms of the clock.

Recently, a ‘phase only’ Kuramoto model [33] was used to propose a mechanism for whole-plant coordination of clocks [8,14]. In order to match experimentally measured rhythms, the model fixed clock periods to different speeds in each region of the plant. It assumed faster rhythms in the cotyledons, hypocotyl, and root tip, and slower rhythms in the rest of the root, as observed experimentally. With these periods fixed, cells were allowed to communicate clock phase through local cell-to-cell coupling. With these assumptions, simulations of the model generated waves of clock gene expression up and down the root, as observed experimentally [8,14]. Thus, local cell-to-cell coupling could enable coordination between organs in plants.

Multiple questions remain about how the plant clock coordinates rhythms that cannot be addressed using a ‘phase only’ model. For example, how are the periods set differently in different parts of the plant? What molecular mechanisms allow the coupling of clock rhythms from cell-to-cell? How can the plant clock network ‘filter’ both internal and environmental noise to robustly entrain to the environment? To begin to address these questions, in this work we developed a spatial network model of the plant circadian system. We modified a previously generated simplified network model and implemented it on a multicellular template of a plant. In our model, the sensitivity to light varies across the plant, and cells communicate via the mRNA levels of a core clock gene. Simulations capture the organ specific period differences and spatial waves observed under LL, demonstrating a plausible mechanism of circadian coordination. We then applied our model to examine how the system keeps time under noisy light-dark (LD) cycles. We found that regional differences persist even under LD cycles, but cell-to-cell minimized differences between neighbor cells. Thus, the combination of local sensitivity to inputs and cell-to-cell coupling allows for coordinated timing in noisy environments.

Results

A locally coupled spatial model of the plant circadian clock network

We first implemented a reduced network model of the *Arabidopsis thaliana* circadian clock [31]. To decrease the complexity of the model, the authors grouped functionally similar genes into single entities (Fig 1A). The compact network model incorporates known light inputs to the network and qualitatively recapitulates clock dynamics under both light dark cycles and constant light. At only 9 equations and 34 parameters the model is also computationally tractable for spatial simulations. We modified the De Caluwe model to include a repression rather than activation interaction between *PSEUDO-RESPONSE REGULATOR 9 (PRR9)*/*PRR7* and *CIRCADIAN CLOCK ASSOCIATED 1* (*CCA1*) / *LATE ELONGATED HYPOCOTYL* (*LHY*), as this has recently been shown experimentally [32,34] (Methods).

We implemented the modified De Caluwe model on a simplified template of a seedling. The template consisted of approximately 800 cells, classified into cotyledon, hypocotyl, root, and root tip regions (Fig 1B and Methods). Although a number of studies have demonstrated local cell-to-cell coupling between clocks in *A. thaliana* [8,11,14,16,18–20], the identity of the coupling components are unclear. Initially, to model the coupling (Fig 1C), the level of *CCA1*/*LHY* in one cell was assumed to be locally coupled to the level of the cell's neighbors. The coupling strength was set to 2 (Methods). To simulate the variability observed in single cell clock rhythms [8] we multiplied the level of each mRNA and protein by a time scaling parameter that was randomly selected from a normal distribution (Methods). The range of this normal distribution was set differently for each organ to qualitatively match the variability observed experimentally (S1 Fig).

Different light sensitivities can explain organ differences in phase and period

129 We next attempted to recapitulate in our model the differences in clock period and phase in
130 different organs that have been observed in experiments using a single cell CCA1-YFP reporter
131 [8] and a *GIGANTEA* luciferase reporter [14]. In these experiments, faster rhythms were
132 observed in the cotyledon, hypocotyl, and root tip, with slower rhythms in the rest of the root.
133 We first reanalyzed existing luciferase data [14] and confirmed that these relationships held for
134 several of the core clock genes in our model, *PSEUDO-RESPONSE REGULATOR 9* (*PRR9)*,
135 *TIMING OF CAB EXPRESSION 1* (*TOC1*), and *EARLY FLOWERING 4* (*ELF4*) (Fig 2A).
136 Whereas in our previous 'phase only' model, we fixed the periods to be different in each part of
137 the plant, with our spatial network model, we could now investigate what causes the differences
138 in periods. Previously it has been hypothesized that different sensitivities to environmental
139 inputs alter periods across the plant [13,14]. For example, cells in the cotyledon may be fast
140 because they are more sensitive to light. Experimental tests of this, however, are confounded by
141 changes in metabolism and development caused by light [35]. To test this in our model, we
142 simulated differences in sensitivity by setting the intensity of light input in our model to differ
143 depending on the region, and examined whether this can generate the period differences
144 observed across the plant.
145
146 We entrained the cells in our simulations to LD cycles for 4 days before releasing them into LL
147 for a further 6 days and measured the periods, as carried out in previous experiments [14].
148 When assuming high sensitivity to light in the cotyledon (L = 1.35) and hypocotyl (L = 1.10), but
149 lower in the root (L = 0.90) and root tip (L = 1.03), all organs entrained to the LD cycles (S2 Fig).
150 Upon transfer to LL, we were able to generate different periods (Fig 2B) and phases (Fig 2D–F
151 and S3 Fig) in each organ, matching those observed experimentally. Thus, our results revealed
152 that different sensitivities to environmental inputs are sufficient to generate the experimentally
153 observed spatial differences in period and phase across the plant. This is due to higher light

154 sensitivity causing the clock to run faster in our simulations (S4 Fig), as expected for a diurnal
155 organism [36].
156
157 **Local sharing of clock mRNA levels can drive spatial waves of clock gene expression**
158 Previously we observed two waves of clock gene expression, one travelling up, and one down
159 the root, in *CCA1*, *PRR9* and *GI* reporters [8,14]. These waves could be explained in a phase
160 only model by cell-to-cell coupling [8,14,19,20]. We next tested whether a plausible mechanism
161 for local cell-to-cell coupling, sharing of mRNA between cells [37], can recapitulate the
162 experimental observations. To provide a benchmark, we first analyzed the seedlings carrying
163 transcriptional reporters for *TOC1*, *PRR9*, and *ELF4* [14] at the sub-tissue level (Methods). As in
164 previous studies, space-time plots revealed spatial waves of gene expression within and
165 between organs for all three genes (Fig 3A and S5 Fig). The direction of the waves can be
166 clearly observed in plots of the final peaks of expression (Fig 3B and S5 Fig). For each gene,
167 the wave patterns appeared similar, with two waves of clock gene expression in the root (Fig
168 3C, S5 Fig, and S1 Video).
169
170 We next analyzed simulations at the sub-tissue level (S6 Fig and Methods) to see if our model
171 captures these spatial dynamics. For each gene, the wave patterns appeared similar to
172 experiments, travelling from the fast oscillating regions that are more sensitive to light, into the
173 slower regions with lower sensitivity to light (Fig 3C, D, S5 Fig and S2 Video). These waves
174 required cell-to-cell coupling through the local sharing of clock mRNA, as we only observed
175 waves with coupling strengths, *J*, above approximately 1 (Fig 3E and S7 Fig). Similar simulation
176 results were obtained using different clock genes as the coupling component, suggesting that
177 any cell-to-cell sharing of clock components can explain the experimentally observed spatial
178 dynamics (S8 Fig). We also found that our simulation results were qualitatively similar when
179 keeping regional differences of light sensitivity and local cell-to-cell coupling, but assuming no

180 cell-to-cell variability within regions (S9 Fig). Additionally, we ran simulations assuming longer
181 distance and global coupling. Increasing the local coupling to be between 8 rather than 4
182 neighbor cells gave qualitatively similar results. However, with global coupling all cells adopted
183 the same phase at higher coupling strengths, regardless of position in the plant (S10 Fig).
184 Finally, by setting the light inputs in our locally coupled model to be equal in all regions of the
185 seedling, we were also able to simulate the loss of waves observed in the light sensing mutant
186 *phyb-9* [14] (S11 Fig). Taken together, these results show that the assumptions of local cell-to-
187 cell coupling and differential light sensitivity between regions are the key aspects of our model
188 that allow a match to experimental data.
189
190 **Local flexibility persists under idealized and noisy LD cycles**
191 Our modelling suggests that different sensitivities to environmental inputs across the plant
192 allows the clock to be locally flexible under LL, by allowing it to adopt different periods and
193 phases across the plant even under the same environment. We simulated our model under LD
194 cycles to investigate whether local flexibility persisted with rhythmic input. We first simulated
195 idealized LD cycles, where lights are switched fully on during the daytime and off at night (Fig
196 4A and Methods). The sensitivity to light during the daytime differed depending on the region, as
197 with LL simulations. We first simulated clock rhythms assuming no cell-to-cell coupling. In the
198 absence of cell-to-cell coupling, close inspection of the final peaks of expression revealed small
199 differences in the timing between regions. *PRR5*/*TOC1* expression in cells of the cotyledon
200 peaked at 132.70 ± 0.50 h (median ± interquartile range), followed by those in the hypocotyl
201 (133.40 ± 0.40 h) and then the root, with cells at the tip (133.50 ± 1.35 h) peaking before those
202 in the middle region of the root (134.80 ± 1.20 h; Fig 4B, left and S12 Fig). These phase
203 differences were qualitatively the same as observed under LL (Fig 2 and 3) but were
204 discontinuous between regions. With the addition of cell-to-cell coupling, the phase differences
205 between regions were no longer discontinuous and were instead staggered, causing the

206 emergence of spatial waves (Fig 4B, middle and right, and S12 Fig). However, phase
207 differences between the regions persisted and did not reduce in size with increasing strengths
208 of coupling (S12 Fig). For example, there was a difference between the cotyledon and root of
209 1.90 ± 0.18 h (median ± interquartile range) without coupling (J = 0), 2.00 ± 0.20 h with coupling
210 (J = 2), and 2.00 ± 0.18 h with stronger coupling (J = 4). A similar spatial structure was observed
211 in *CCA1*/*LHY* and *PRR7*/*PRR9* expression (S12 Fig). However, *ELF4*/*LUX* appeared more
212 synchronized when the peak coincided with the dark transition, as darkness causes strong
213 repression of *ELF4* expression.
214
215 We next simulated more realistic LD cycles containing fluctuations in the light intensity (Fig 4C).
216 These LD cycles were designed to approximate the differences in input that cells may
217 experience due to weather or a cell's microenvironment (Methods). Examination of the times of
218 the final peaks of expression reveals large variation in peak times within regions when cell-to-
219 cell coupling was absent (J = 0; Fig 4D, left). This made any difference in phase between
220 regions difficult to resolve. However, with increasing strengths of cell-to-cell coupling we
221 observed a decrease in variability. For example, there was a difference of 5.00 ± 1.05 h (median
222 ± interquartile range) between the earliest and latest peaking cells without coupling (J = 0), but
223 3.10 ± 0.23 h with coupling (J = 2), and 3.20 ± 0.15 h with stronger coupling (J = 4). This
224 decrease in cell-to-cell variation revealed an underlying spatial structure (Fig 4D, middle and
225 right, and S13 Fig), comparable to that observed under idealized LD cycles (Fig 4B, middle and
226 right, and S12 Fig). Phase differences and spatial waves persisted with increasing strengths of
227 coupling (S13 Fig). This spatial structure was also observed in expression of *CCA1*/*LHY* and
228 *PRR7*/*PRR9*, but not in *ELF4*/LUX expression (S13 Fig). Together this shows that local flexibility
229 in phase, and spatial waves, persisted under LD cycles when local cell-to-cell coupling was
230 present.
231

232 **Cell-to-cell coupling maintains global coordination under noisy light-dark cycles**

233 Simulations under noisy LD cycles showed that whilst local flexibility of regions persisted, cell-
234 to-cell coupling decreased the phase variation within regions (Fig 4). We further investigated the
235 function of cell-to-cell coupling by testing whether coupling also affected the global
236 synchronization of rhythms, or is limited to a local effect on rhythms. To test this, we quantified
237 the synchrony between all cells within the template seedling using a score for synchronization,
238 *R* [38]. The synchronization index, *R*, is the ratio of the variance of the average signal to the
239 average variance of the individual cells. When cells are synchronized these variances are equal
240 to each other and *R* becomes 1, whereas when desynchronized *R* becomes 0. For each gene
241 pair, we observed a high *R* value under idealized LD cycles, with or without cell-to-cell coupling
242 (Fig 5, black lines). However, cells were less synchronous under noisy LD cycles (Fig 5, red
243 lines). Each gene showed a reduced level of synchrony in the absence of cell-to-cell coupling (J
244 $= 0$). *PRR9*/*PRR7* was the most affected by the noise, with a synchronization index of 0.97 ±
245 0.002 (mean ± standard deviation) under idealized LD and 0.61 ± 0.008 under noisy LD cycles
246 (Fig 5B). This is likely because *PRR9*/*PRR7* synthesis is most strongly affected by light (Table
247 1).
248
249 We observed an increase in global synchronization under noisy LD cycles as coupling strengths
250 increased (Fig 5). At higher strengths of coupling ($J > 2$), for *CCA1/LHY* and *PRR5/TOC1* the
251 synchronization index under noisy LD cycles approximately equaled that under idealized LD
252 cycles (Fig 5A and C). For *PRR9*/*PRR7* and *ELF4*/*LUX* expression the synchronization index
253 increased with increasing coupling strength, but did not reach the level observed under
254 idealized LD cycles for all coupling strengths tested (Fig 5B and D). Oscillations of protein
255 expression also increased in synchrony with cell-to-cell coupling (S14 Fig). Thus, local cell-to-
256 cell coupling improves the global coordination of circadian timing under noisy light-dark cycles,
257 whilst still allowing differences in clock timing between regions.

258

259 **Discussion**

260 Here we develop a spatial network model for the plant clock and use it to examine the design
261 principles of clock coordination in plants. This simple multicellular model, which assumes
262 regional differences in sensitivity to light and cell-to-cell coupling through the local sharing of
263 clock mRNA levels, successfully simulates the period differences and phase waves across the
264 plant observed under LL in previous time lapse experiments. Our simulations predict that phase
265 flexibility persists under LD cycles, with cell-to-cell coupling reducing cell-to-cell differences but
266 still allowing regional flexibility. We therefore find that the plant circadian clock system can
267 combine regional differences in environmental signaling with cell-to-cell coupling to enable
268 robust, yet flexible, circadian timing under noisy environmental cycles.

269

270 Previous models of the plant circadian clock have proven important for understanding aspects
271 of plant physiology, including starch metabolism and flowering [39,40]. However, it was recently
272 shown that the clock controls physiology in a tissue-specific manner. For example, clocks in the
273 epidermis regulate growth, whereas those in the vasculature regulate flowering [41]. In future,
274 our spatial model could be extended to investigate circadian control of physiology at the cell and
275 tissue level. An interesting example would be cell division, which is regulated by the clock [2],
276 and occurs in meristematic regions of the plant [42]. It will be interesting to see if, and how,
277 flexibility of the circadian system impacts tightly controlled phenotypes such as this.

278

279 Including noise in LD cycles represents a step towards understanding how the plant circadian
280 system works under natural conditions. Our simulations under noisy LD cycles reveal that local
281 cell-to-coupling allows a balance between ensuring cells are coordinated locally even under a
282 noisy environment, whilst still allowing regional differences that would not be possible with a
283 global coupling mechanism. However, this is still a simplification of the real environment. For

284 example, we do not consider temperature, which is phase shifted between the air and soil [43].
285 Although technically challenging, experiments under more realistic conditions such as this will
286 be important for furthering our understanding. Promising advances in this direction include the
287 GLO-Roots system [44], and the robotics of Bordage et al. [13], which allow the root to be
288 imaged in the dark under LD cycles. As experiments progress, we predict that spatial models
289 such as ours will be crucial for understanding how the clock integrates such a range of
290 environmental signals across the plant.
291
292 The molecular details underlying the spatial differences, and coordination, of the plant circadian
293 system are still being deciphered. Recently, *ELF3*, *ELF4*, and *LUX* were found to be central to
294 the difference between the shoot and root, possibly due to their interaction with the light
295 signaling protein PHYB [15]. However, interpretation is hindered by the fact that components
296 causing differences could also act as a cell-to-cell mobile coupling signal. For example, ELF4
297 has also been proposed to move from the shoot to couple with clocks in the root [21]. We note
298 that our spatial molecular model has the potential to delineate these two effects. In future work it
299 will be important to vary the identity of the coupling signal, and the underlying genetic network,
300 to generate testable predictions.
301
302 The plant circadian system, with local inputs to cells that are coupled together, represents a
303 decentralized structure. This is in contrast to the centralized mammalian circadian system [45].
304 Here we found that this decentralized structure can afford plants flexibility, allowing regions to
305 adopt different phases under noisy LD cycles. It could be speculated that this has a
306 physiological effect on plants, causing, for example, a stagger in the timing of growth across the
307 plant. However, further work is required to understand how, or whether, this flexibility is an
308 advantage to plants.
309

Acknowledgements

MG and JL were supported by the Gatsby Charitable Foundation (grant number GAT3395/GLC) and IT by the Japan Society for the Promotion of Science (grant numbers 17H06313, 18H02477, and 20K11875). We thank Dr. Katie Abley (University of Cambridge) for critical reading of the manuscript.

Methods

Single cell molecular model

As a model for the plant circadian clock, we exploit the compact model introduced by De Caluwe et al. [31]. The original compact model consists of 9 ordinary differential equations. Among them, 8 equations describe the temporal evolution of the mRNA and protein levels of the core clock genes. The clock genes are grouped into four sets of lumped pairs labeled as: CL (*CCA1* and *LHY*), P97 (*PRR9* and *PRR7*), P51 (*PRR5* and *TOC1*) and EL (*ELF4* and *LUX*). The 9-th equation is for the light-sensitive protein P (PIF3 and PIL1).

In our modeling, one modification to the original compact model was made. According to the experiments reported in [46], the compact model assumed that the P97 variable is activated by CL. However, more recent work [28,34], has shown that *LHY* acts as a repressor of all other clock components, including *PRR9* and *PRR7*. We therefore replaced the activation term that represents the connection from CL to P97 with a repression. The revised single cell model is now described by the following differential equations:

$$\frac{dc_{CL}^{(m)}}{dt} = \left(v_1 + v_{1L}L(t)c_P^{(p)}\right)\frac{1}{1 + (c_{CL}^{(p)}/K_0)^2 + (c_{P97}^{(p)}/K_1)^2 + (c_{P51}^{(p)}/K_2)^2} - \left(k_{1L}L(t) + k_{1D}D(t)\right)c_{CL}^{(m)},$$

$$\frac{dc_{CL}^{(p)}}{dt} = \left(p_1 + p_{1L}L(t)\right)c_{CL}^{(m)} - d_1 c_{CL}^{(p)},$$

$$\frac{dc_{P97}^{(m)}}{dt} = \left(v_{2L}L(t)c_P^{(p)} + v_{2A}\right)\frac{1}{1 + (c_{P51}^{(p)}/K_4)^2 + (c_{EL}^{(p)}/K_5)^2 + (c_{CL}^{(p)}/K_{5b})^2} - k_2 c_{P97}^{(m)},$$

$$\frac{dc_{P97}^{(p)}}{dt} = p_2 c_{P97}^{(m)} - \left(d_{2D}D(t) + d_{2L}L(t)\right)c_{P97}^{(p)},$$

$$\frac{dc_{P51}^{(m)}}{dt} = v_3 \frac{1}{1 + (c_{CL}^{(p)}/K_6)^2 + (c_{P51}^{(p)}/K_7)^2} - k_3 c_{P51}^{(m)},$$

$$\frac{dc_{P51}^{(p)}}{dt} = p_3 c_{P51}^{(m)} - \left(d_{3D}D(t) + d_{3L}L(t)\right)c_{P51}^{(p)},$$

$$\frac{dc_{EL}^{(m)}}{dt} = L(t)v_4 \frac{1}{1 + (c_{CL}^{(p)}/K_8)^2 + (c_{P51}^{(p)}/K_9)^2 + (c_{EL}^{(p)}/K_{10})^2} - k_4 c_{EL}^{(m)},$$

$$\frac{dc_{EL}^{(p)}}{dt} = p_4 c_{EL}^{(m)} - \left(d_{4D}D(t) + d_{4L}L(t)\right)c_{EL}^{(p)},$$

$$\frac{dc_P^{(p)}}{dt} = 0.3\left(1 + c_P^{(p)}\right)D(t) - c_P^{(p)}L(t).$$

$c_\alpha^{(m)}$ and $c_\alpha^{(p)}$ represent the concentration of the α-th mRNA and protein (or protein complex) respectively, for α = CL, P97, P51, EL, and P. *L*(t) represents the input light signal (*L* = 0, lights off; *L* > 0, lights on) and *D(t)* denotes a corresponding darkness input signal (*D* = 1, lights off; *D* = 0, lights on). The model contains 34 parameters, the values of which have been obtained previously through automated optimization [31]. The parameter values for $\boldsymbol{K_0}, \boldsymbol{K_4}, \boldsymbol{K_5}, \boldsymbol{K_{5b}}$ related to the modified interaction from CL to P97 were optimized by minimizing the cost function detailed in the following subsection. Sobol search and simulated annealing were combined to optimize within the range $\boldsymbol{K_i} \in [\boldsymbol{0.1}, \boldsymbol{10}]$ for $i = 0,4,5,5b$. The optimized parameter values together with the original values determined by De Caluwe et al. [31] are listed in S1 Table. The free running periods of the revised model are 25.5 h (LL; L = 1) and 26.25 h (DD; D = 1). Under LD cycles, peak times (ZT) of the gene expressions were CL = 0.50 h, P97 = 8.25 h, P51 = 17.50 h, and EL = 11.75 h.

353 **Cost function**

354 In the parameter optimization of the single cell model, the cost function was computed as
355 follows. First, the model was simulated under 12-h light–12-h dark conditions for a total of 60
356 days and then released into LL for 60 days, followed by constant dark (DD) for 60 days. In each
357 light condition, the first 55 days were discarded as a transient dynamic. To ensure detectable
358 rhythmicity under LL and DD conditions, all variables were required to have a minimum
359 value of 0.1, as well as a minimum difference of 10 % between their minimum and maximum
360 values. Any solution that did not meet these criteria was penalized with an arbitrarily large
361 score. Then, the free-running period was calculated using the chi-square periodogram [47] from
362 CL gene expression, at a significance level of 1 %. A score of 0 was given to a solution having a
363 free-running period between 24 and 25 h under LL and between 25 and 28 h under DD.
364 Solutions with free-running periods outside these ranges were allocated the scores of $(\tau_{LL} -$
365 $24.5)^2/(0.1 \cdot 24.5)^2$ and $(\tau_{DD} - 26.5)^2/(0.1 \cdot 26.5)^2$, where τ_{LL} and τ_{DD} represent free-running
366 periods under LL and DD, respectively. For simulations under 12-h light–12-h dark cycles,
367 solutions that were not entrained to the LD cycles were penalized with an arbitrarily large score.
368 Entrained solutions were given a score of 0 for each gene that attained peak expression within $\pm$
369 1 h of the expected ZT, which were as follows: CL = 1.5, P97 = 6, P51 = 12, and EL = 9.
370 Expression peaks lying outside these intervals were scored as $(ZT_{CL} - 1.5)^2/(0.1 \cdot 24)^2$,
371 $(ZT_{P97} - 6)^2/(0.1 \cdot 24)^2$, $(ZT_{P51} - 12)^2/(0.1 \cdot 24)^2$, $(ZT_{EL} - 9)^2/(0.1 \cdot 24)^2$, where ZT_α denotes
372 Zeitgeber time of the α-th gene's peak expression.

373

374 **Spatial molecular model**

375 To simulate the spatial dynamics, we implemented the revised model on a simplified template of
376 a plant. The template consisted of approximately 800 cells, classified into cotyledon, hypocotyl,
377 root, and root tip regions (Fig 1B). Each cell contained an implementation of the revised

compact model. To simulate growth of the seedlings, we added a row of cells to the root tip every 24 h. During this growth, the root tip region of the template was kept fixed in size. To do this, after the addition of new cells, the previously uppermost root tip cells became root cells instead.

As the coupling agents have yet to be clearly identified by experimental studies, the individual cells are assumed to be coupled through CL. Our model for coupled plant cells is described as follows:

$$\tau_i \frac{dc_{CL,i}^{(m)}}{dt} = \left(v_1 + v_{1L}L(t)c_{P,i}^{(p)}\right)\frac{1}{1+(c_{CL,i}^{(p)}/K_0)^2+(c_{P97,i}^{(p)}/K_1)^2+(c_{P51,i}^{(p)}/K_2)^2}$$

$$-\left(k_{1L}L(t)+k_{1D}D(t)\right)c_{CL,i}^{(m)} + J\left(\bar{c}_{CL,i}^{(m)} - c_{CL,i}^{(m)}\right),$$

$$\tau_i \frac{dc_{CL,i}^{(p)}}{dt} = \left(p_1 + p_{1L}L(t)\right)c_{CL,i}^{(m)} - d_1 c_{CL,i}^{(p)},$$

$$\tau_i \frac{dc_{P97,i}^{(m)}}{dt} = \left(v_{2L}L(t)c_{P,i}^{(p)} + v_{2A}\right)\frac{1}{1+(c_{P51,i}^{(p)}/K_4)^2+(c_{EL,i}^{(p)}/K_5)^2+(c_{CL,i}^{(p)}/K_{5b})^2} - k_2 c_{P97,i}^{(m)},$$

$$\tau_i \frac{dc_{P97,i}^{(p)}}{dt} = p_2 c_{P97,i}^{(m)} - \left(d_{2D}D(t) + d_{2L}L(t)\right)c_{P97,i}^{(p)},$$

$$\tau_i \frac{dc_{P51,i}^{(m)}}{dt} = v_3 \frac{1}{1+(c_{CL,i}^{(p)}/K_6)^2+(c_{P51,i}^{(p)}/K_7)^2} - k_3 c_{P51,i}^{(m)},$$

$$\tau_i \frac{dc_{P51,i}^{(p)}}{dt} = p_3 c_{P51,i}^{(m)} - \left(d_{3D}D(t) + d_{3L}L(t)\right)c_{P51,i}^{(p)},$$

$$\tau_i \frac{dc_{EL,i}^{(m)}}{dt} = L(t)v_4 \frac{1}{1+(c_{CL,i}^{(p)}/K_8)^2+(c_{P51,i}^{(p)}/K_9)^2+(c_{EL,i}^{(p)}/K_{10})^2} - k_4 c_{EL,i}^{(m)},$$

$$\tau_i \frac{dc_{EL,i}^{(p)}}{dt} = p_4 c_{EL,i}^{(m)} - \left(d_{4D}D(t) + d_{4L}L(t)\right)c_{EL,i}^{(p)},$$

$$\tau_i \frac{dc_{P,i}^{(p)}}{dt} = 0.3\left(1 + c_{P,i}^{(p)}\right)D(t) - c_{P,i}^{(p)}L(t).$$

396 As in the revised single cell model, $c_\alpha^{(m)}$ and $c_\alpha^{(p)}$ represent the concentration of the α-th mRNA
397 and protein (or protein complex) respectively for α = CL, P97, P51, EL, and P, in the i-th cell
398 ($i = 1, 2, \ldots, N$). In the first equation, the CL gene is locally and diffusively coupled to its
399 neighboring cells, where J is the coupling strength and $\bar{c}_{CL,i}^{(m)} = \frac{1}{4}\sum_{j\in N(i)} c_{CL,j}^{(m)}$ represents averaged
400 expression level over 4 neighboring cells (left, right, above, and below). In the case of coupling
401 between 8 neighboring cells (left, right, above, below, left above, left below, right above, and
402 right below), the averaged expression level becomes $\bar{c}_{CL,i}^{(m)} = \frac{1}{8}\sum_{j\in N(i)} c_{CL,j}^{(m)}$, or $\bar{c}_{CL,i}^{(m)} = \frac{1}{N}\sum_{j=1}^{N} c_{CL,j}^{(m)}$
403 for the case of globally coupled cells. The coupling strength was set to $J = 0, 0.001, 0.01, 0.1, 1, 2,$
404 or 4.
405
406 **Differential light input to cells**
407 We set the light strength, *L*, to vary depending on the position of the cell. In doing so, we found
408 that modest differences in *L* were sufficient to generate period differences between regions. To
409 approximate the period differences that we observed between regions in experiments (Fig 2A)
410 we set *L* = 1.35 for cotyledon cells, *L* = 1.10 for hypocotyl cells, *L* = 0.90 for root cells, and *L* =
411 1.03 for root tip cells. As the template of the seedling grew, we kept the root tip region of fixed
412 size (see 'Spatial molecular model'). This meant that the uppermost root tip cells become root
413 cells instead. After this transition, the light input decreased so that cells received a level
414 characteristic of root cells, *L* = 0.90. This caused these cells to slow.
415
416 To generate cell-to-cell variability in periods, the time scaling parameters τ_i were set according
417 to normal distributions as N(1, 0.059), N(1, 0.028), N(1, 0.073), N(1, 0.089) for the four regions,
418 as informed by the analysis of single cell data [8]. For these values of *L* and τ_i, the intrinsic
419 periods of the 4 regions ($J = 0$) in the absence of growth were 23.2 $\pm$ 1.4 h, 25.5 $\pm$ 0.7 h, 27.9
420 $\pm$ 2.0 h, and 26.3 $\pm$ 2.3 h (mean $\pm$ standard deviation) respectively.

421

422 **Characterizing clock periods from experiments**

423 We analyzed experimental luciferase and confocal data to characterize the periods within a
424 seedling. We previously completed an organ-level analysis of period and phase for *PRR9*::*LUC*,
425 *ELF4*::*LUC*, and *TOC1*::*LUC* expression [14]. In this analysis, 315 μm diameter regions of
426 interest (ROI) were defined to represent the cotyledon, hypocotyl, root, and root tip regions of
427 the seedling. These ROI were used to generate time series, from which period estimates were
428 made across a number of individual seedlings. Here, we pooled estimates made from
429 *PRR9*::*LUC*, *ELF4*::*LUC*, and *TOC1*::*LUC* lines, and calculated the mean for each region (Fig
430 2A). Only periods from time series classified as rhythmic (as defined previously [14]) were used
431 in the calculation.

432

433 To characterize the variability of the periods, we measured the between-cell variation of clock
434 periods in each region of the plant (S1 Fig). To do this we analyzed a dataset of single cell time-
435 lapse microscopy, CCA1-YFP translational fusion data [8]. We defined cells as being within the
436 root tip region if they are less than 315 μm from the most distal cell of the root tip. Where there
437 are multiple imaging sections in the same organ, cells are pooled to give one region for the
438 cotyledon, hypocotyl, and root. Variability was estimated using the coefficient of variation (CV;
439 standard deviation / mean) of all cells within these regions. Only periods from time series
440 classified as rhythmic (as defined previously [8]) were used in the calculation.

441

442 **Organ-level analysis**

443 To assess our model we quantified the times of the peaks of expression. For experimental data,
444 we used the ROI positions defined previously [14]. For the model, we defined 5-by-3 (width-by-
445 height) pixel ROI on the seedling template, approximating the positions used in the experimental
446 analysis of (S6 Fig). The mean of these ROI at each time point were taken to give the simulated

447 time series. Peaks within 24–144 h after transfer to LL were identified using the “findpeaks”
448 MATLAB (MathWorks, UK) function, with the constraint that peaks must be more than 19 h
449 apart. For visual clarity, only peaks in which all organs completed the full cycle within the time
450 window were plotted. Peaks of simulated expression were plotted against previously published
451 experimental data for comparison (e.g. Fig 2D–F) [14]. Only peaks from experimental time
452 series classified as rhythmic (as defined previously [14]) were plotted.
453
454 **Space-time plots**
455 To visualize the spatial clock dynamics, we created space-time plots of gene expression (e.g.
456 Fig 3A). We made plots of *PRR9*::*LUC*, *ELF4*::*LUC*, and *TOC1*::*LUC* expression as described
457 previously [14]. Individual time series of the space-time plots were background subtracted and
458 small gaps caused by segmentation errors were interpolated. A third-order Butterworth filter was
459 then applied to reduce the high frequency noise. To create space-time plots of simulated clock
460 gene expression, we also extracted the expression from sections that are perpendicular to the
461 primary axis of the seedling (S6 Fig). We take the mean expression from 1-by-5 cell cross-
462 sections of the template. To aid interpretation of space-time plots, amplitude trends were
463 removed from both experimental and model space-time plots using part of the mFourFit
464 algorithm [25].
465
466 We additionally plotted the times of the final peaks of expression of the space-time plots (e.g.
467 Fig 3B). The final oscillation in which all organs completed the full cycle was used. We detected
468 peaks within a 24 h window of the expected time of these peaks. If more than one peak was
469 detected, we plotted the peak with the highest height.
470
471 **Entrainment to noisy LD cycles**

472 We modelled entrainment by simulating light cycles with a day length of 12 h. The level of light
473 during the day varied depending on the region of the template, matching *L* values under LL. We
474 termed these cycles without noise 'idealized LD' (Fig 4A). To simulate fluctuations in the light
475 cycle we utilized an algorithm developed previously [48], which approximates meteorological
476 data [49]. Fluctuations lasted a random interval of time drawn from an exponential distribution of
477 mean 2.4 h. The intensity of light during each fluctuation was drawn from a second uniform
478 distribution of the range 0 to L_{max}, with L_{max} matching the *L* values for the cell under LL. The
479 values are set according to the position of the cell on the template, as under LL. We termed this
480 condition 'noisy LD' (Fig 4D). We made the simplifying assumption that each cell is exposed to
481 an independent noisy LD cycle due to their unique positions in the environment. LD cycles were
482 input to the molecular model through the parameter *L*.
483
484 **Synchrony analysis**
485 We estimated the global synchrony in simulations from the variance of the individual cells (Fig 5
486 and S14 Fig). Firstly, the average signal of all *N* cells of the simulation $\{x_h(t)$: $h = 1, 2, ..., N\}$,
487 was computed as $M(t) = \frac{1}{N}\sum_{h=0}^{N} x_h(t)$. Then the overall level of synchrony was measured by
488 the synchronization index [38],

489 $$R = \frac{\langle M^2 \rangle - \langle M \rangle^2}{\frac{1}{N}\sum_h^N \{\langle x_h{}^2 \rangle - \langle x_h \rangle^2},$$

490 where ⟨⟩ denotes the time average, which in our case was between 0 and 144 h. The
491 synchronization index measures the ratio of the variance of the average signal to the average
492 variance of the individual cells. The parameter quantifies the distribution of both the phases and
493 amplitudes of the individual cells. However, we normalized the individual traces to remove
494 amplitude variance and therefore measured only the phase differences. *R* ranges from 1 when
495 cells are synchronized, to 0 when cells are completely desynchronized.

496

497 **References**

498 1. Webb AAR, Seki M, Satake A, Caldana C. Continuous dynamic adjustment of the plant
499 circadian oscillator. Nat Commun. 2019;10: 550. doi:10.1038/s41467-019-08398-5
500 2. Fung-Uceda J, Lee K, Seo PJ, Polyn S, De Veylder L, Mas P. The Circadian Clock Sets
501 the Time of DNA Replication Licensing to Regulate Growth in Arabidopsis. Dev Cell.
502 2018;45: 101–113. doi:10.1016/j.devcel.2018.02.022
503 3. Nozue K, Covington MF, Duek PD, Lorrain S, Fankhauser C, Harmer SL, et al. Rhythmic
504 growth explained by coincidence between internal and external cues. Nature. 2007;448:
505 358–361. doi:10.1038/nature05946
506 4. Fenske MP, Nguyen LP, Horn EK, Riffell JA, Imaizumi T. Circadian clocks of both plants
507 and pollinators influence flower seeking behavior of the pollinator hawkmoth Manduca
508 sexta. Sci Rep. 2018;8: 2842. doi:10.1038/s41598-018-21251-x
509 5. Greenwood M, Locke JC. The circadian clock coordinates plant development through
510 specificity at the tissue and cellular level. Curr Opin Plant Biol. 2020;53: 65–72.
511 doi:10.1016/j.pbi.2019.09.004
512 6. Dodd AN, Salathia N, Hall A, Kevei E, Toth R, Nagy F, et al. Plant Circadian Clocks
513 Increase Photosynthesis, Growth, Survival, and Competitive Advantage. Science.
514 2005;309: 630–633. doi:10.1126/science.1115581
515 7. Green RM, Tingay S, Wang Z-Y, Tobin EM. Circadian rhythms confer a higher level of
516 fitness to Arabidopsis plants. Plant Physiol. 2002;129: 576–84. doi:10.1104/pp.004374
517 8. Gould PD, Domijan M, Greenwood M, Tokuda IT, Rees H, Kozma-Bognar L, et al.
518 Coordination of robust single cell rhythms in the Arabidopsis circadian clock via spatial
519 waves of gene expression. Elife. 2018;7: e31700. doi:10.7554/eLife.31700
520 9. Thain SC, Murtas G, Lynn JR, McGrath RB, Millar AJ. The circadian clock that controls
521 gene expression in Arabidopsis is tissue specific. Plant Physiol. 2002;130: 102–110.

522 doi:10.1104/pp.005405
523 10. Yakir E, Hassidim M, Melamed-Book N, Hilman D, Kron I, Green RM. Cell autonomous
524 and cell-type specific circadian rhythms in Arabidopsis. Plant J. 2011;68: 520–531.
525 doi:10.1111/j.1365-313X.2011.04707.x
526 11. Takahashi N, Hirata Y, Aihara K, Mas P. A Hierarchical Multi-oscillator Network
527 Orchestrates the Arabidopsis Circadian System. Cell. 2015;163: 148–159.
528 doi:10.1016/j.cell.2015.08.062
529 12. James AB, Monreal JA, Nimmo GA, Kelly CL, Herzyk P, Jenkins GI, et al. The circadian
530 clock in Arabidopsis roots is a simplified slave version of the clock in shoots. Science.
531 2008;322: 1832–5. doi:10.1126/science.1161403
532 13. Bordage S, Sullivan S, Laird J, Millar AJ, Nimmo HG. Organ specificity in the plant
533 circadian system is explained by different light inputs to the shoot and root clocks. New
534 Phytol. 2016;212: 136–49. doi:10.1111/nph.14024
535 14. Greenwood M, Domijan M, Gould PD, Hall AJW, Locke JCW. Coordinated circadian
536 timing through the integration of local inputs in Arabidopsis thaliana. PLoS Biol. 2019;17:
537 e3000407. doi:https://doi.org/10.1371/journal.pbio.3000407
538 15. Nimmo HG, Laird J, Bindbeutel R, Nusinow DA. The evening complex is central to the
539 difference between the circadian clocks of Arabidopsis thaliana shoots and roots. Physiol
540 Plant. 2020; ppl.13108. doi:10.1111/ppl.13108
541 16. Endo M, Shimizu H, Nohales MA, Araki T, Kay SA. Tissue-specific clocks in Arabidopsis
542 show asymmetric coupling. Nature. 2014;515: 419–422. doi:10.1038/nature13919
543 17. Lee HG, Seo PJ. Dependence and independence of the root clock on the shoot clock in
544 Arabidopsis. Genes Genomics. 2018;40: 1063–1068. doi:10.1007/s13258-018-0710-4
545 18. Wenden B, Toner DLK, Hodge SK, Grima R, Millar AJ. Spontaneous spatiotemporal
546 waves of gene expression from biological clocks in the leaf. Proc Natl Acad Sci U S A.
547 2012;109: 6757–6762. doi:10.1073/pnas.1118814109

19. Fukuda H, Nakamichi N, Hisatsune M, Murase H, Mizuno T. Synchronization of Plant Circadian Oscillators with a Phase Delay Effect of the Vein Network. Phys Rev Lett. 2007;99: 098102. doi:10.1103/PhysRevLett.99.098102

20. Fukuda H, Ukai K, Oyama T. Self-arrangement of cellular circadian rhythms through phase-resetting in plant roots. Phys Rev E. 2012;86: 041917. doi:10.1103/PhysRevE.86.041917

21. Chen WW, Takahashi N, Hirata Y, Ronald J, Porco S, Davis SJ, et al. A mobile ELF4 delivers circadian temperature information from shoots to roots. Nat Plants. 2020;6: 416–426. doi:10.1038/s41477-020-0634-2

22. Nimmo HG. Entrainment of Arabidopsis roots to the light:dark cycle by light piping. Plant Cell Environ. 2018;41: 1742–1748. doi:10.1111/pce.13137

23. Locke JCW, Southern MM, Kozma-Bognár L, Hibberd V, Brown PE, Turner MS, et al. Extension of a genetic network model by iterative experimentation and mathematical analysis. Mol Syst Biol. 2005;1: 2005.0013. doi:10.1038/msb4100018

24. Locke JCW, Kozma-Bognár L, Gould PD, Fehér B, Kevei E, Nagy F, et al. Experimental validation of a predicted feedback loop in the multi-oscillator clock of Arabidopsis thaliana. Mol Syst Biol. 2006;2: 59. doi:10.1038/msb4100102

25. Edwards KD, Akman OE, Knox K, Lumsden PJ, Thomson AW, Brown PE, et al. Quantitative analysis of regulatory flexibility under changing environmental conditions. Mol Syst Biol. 2010;6: 424. doi:10.1038/MSB.2010.81

26. Pokhilko A, Hodge SK, Stratford K, Knox K, Edwards KD, Thomson AW, et al. Data assimilation constrains new connections and components in a complex, eukaryotic circadian clock model. Mol Syst Biol. 2010;6: 416. doi:10.1038/msb.2010.69

27. Pokhilko A, Fernández AP, Edwards KD, Southern MM, Halliday KJ, Millar AJ. The clock gene circuit in Arabidopsis includes a repressilator with additional feedback loops. Mol Syst Biol. 2012;8: 574. doi:10.1038/msb.2012.6

574 28. Fogelmark K, Troein C. Rethinking transcriptional activation in the Arabidopsis circadian
575 clock. PLoS Comput Biol. 2014;10: e1003705. doi:10.1371/journal.pcbi.1003705
576 29. Akman OE, Watterson S, Parton A, Binns N, Millar AJ, Ghazal P. Digital clocks: simple
577 Boolean models can quantitatively describe circadian systems. J R Soc Interface. 2012;9:
578 2365–2382. doi:10.1098/rsif.2012.0080
579 30. Foo M, Somers DE, Kim P-J. Kernel Architecture of the Genetic Circuitry of the
580 Arabidopsis Circadian System. Jensen LJ, editor. PLoS Comput Biol. 2016;12:
581 e1004748. doi:10.1371/journal.pcbi.1004748
582 31. De Caluwé J, Xiao Q, Hermans C, Verbruggen N, Leloup J-C, Gonze D. A Compact
583 Model for the Complex Plant Circadian Clock. Front Plant Sci. 2016;7: 74.
584 doi:10.3389/fpls.2016.00074
585 32. Tokuda IT, Akman OE, Locke JCW. Reducing the complexity of mathematical models for
586 the plant circadian clock by distributed delays. J Theor Biol. 2019;463: 155–166.
587 doi:10.1016/J.JTBI.2018.12.014
588 33. Kuramoto Y. Self-entrainment of a population of coupled non-linear oscillators.
589 International Symposium on Mathematical Problems in Theoretical Physics.
590 Berlin/Heidelberg: Springer-Verlag; 1975. pp. 420–422. doi:10.1007/bfb0013365
591 34. Adams S, Manfield I, Stockley P, Carre IA, Dowidar N, Dunaway D. Revised Morning
592 Loops of the Arabidopsis Circadian Clock Based on Analyses of Direct Regulatory
593 Interactions. Foulkes NS, editor. PLoS One. 2015;10: e0143943.
594 doi:10.1371/journal.pone.0143943
595 35. Taiz L, Zeiger E, Møller IM, Murphy A. Plant Physiology and Development. 6th ed.
596 Sunderland: Sinauer Associates; 2018.
597 36. Aschoff J, Pohl H. Phase relations between a circadian rhythm and its zeitgeber within
598 the range of entrainment. Naturwissenschaften. 1978;65: 80–4. doi:10.1007/BF00440545
599 37. Maizel A, Markmann K, Timmermans M, Wachter A. To move or not to move: roles and

600 specificity of plant RNA mobility. Curr Opin Plant Biol. 2020;57: 52–60.
601 doi:10.1016/j.pbi.2020.05.005
602 38. Garcia-Ojalvo J, Elowitz MB, Strogatz SH. Modeling a synthetic multicellular clock:
603 repressilators coupled by quorum sensing. Proc Natl Acad Sci U S A. 2004;101: 10955–
604 60. doi:10.1073/pnas.0307095101
605 39. Seaton DD, Ebenhöh O, Millar AJ, Pokhilko A. Regulatory principles and experimental
606 approaches to the circadian control of starch turnover. J R Soc Interface. 2014;11:
607 20130979. doi:10.1098/rsif.2013.0979
608 40. Seaton DD, Smith RW, Song YH, MacGregor DR, Stewart K, Steel G, et al. Linked
609 circadian outputs control elongation growth and flowering in response to photoperiod and
610 temperature. Mol Syst Biol. 2015;11: 776. doi:10.15252/MSB.20145766
611 41. Shimizu H, Katayama K, Koto T, Torii K, Araki T, Endo M. Decentralized circadian clocks
612 process thermal and photoperiodic cues in specific tissues. Nat Plants. 2015;1: 15163.
613 doi:10.1038/nplants.2015.163
614 42. Meyerowitz EM. Genetic control of cell division patterns in developing plants. Cell.
615 1997;88: 299–308. doi:10.1016/S0092-8674(00)81868-1
616 43. Dawson GB, Fisher RG. Diurnal and seasonal ground temperature variations at Wairakei.
617 New Zeal J Geol Geophys. 1964;7: 144–154. doi:10.1080/00288306.1964.10420166
618 44. Rellán-Álvarez R, Lobet G, Lindner H, Pradier P-L, Sebastian J, Yee M-C, et al. GLO-
619 Roots: an imaging platform enabling multidimensional characterization of soil-grown root
620 systems. Elife. 2015;4. doi:10.7554/eLife.07597
621 45. Bell-Pedersen D, Cassone VM, Earnest DJ, Golden SS, Hardin PE, Thomas TL, et al.
622 Circadian rhythms from multiple oscillators: lessons from diverse organisms. Nat Rev
623 Genet. 2005;6: 544–556. doi:10.1038/nrg1633
624 46. Para A, Farré EM, Imaizumi T, Pruneda-Paz JL, Harmon FG, Kay SA. PRR3 Is a
625 vascular regulator of TOC1 stability in the Arabidopsis circadian clock. Plant Cell.

2007;19: 3462–73. doi:10.1105/tpc.107.054775

47. Sokolove PG, Bushell WN. The chi square periodogram: Its utility for analysis of circadian rhythms. J Theor Biol. 1978;72: 131–160. doi:10.1016/0022-5193(78)90022-X

48. Pittayakanchit W, Lu Z, Chew J, Rust MJ, Murugan A. Biophysical clocks face a trade-off between internal and external noise resistance. Elife. 2018;7. doi:10.7554/eLife.37624

49. Gu L, Fuentes JD, Garstang M, Silva JT Da, Heitz R, Sigler J, et al. Cloud modulation of surface solar irradiance at a pasture site in Southern Brazil. Agric For Meteorol. 2001;106: 117–129. doi:10.1016/S0168-1923(00)00209-4

652 **Figures**

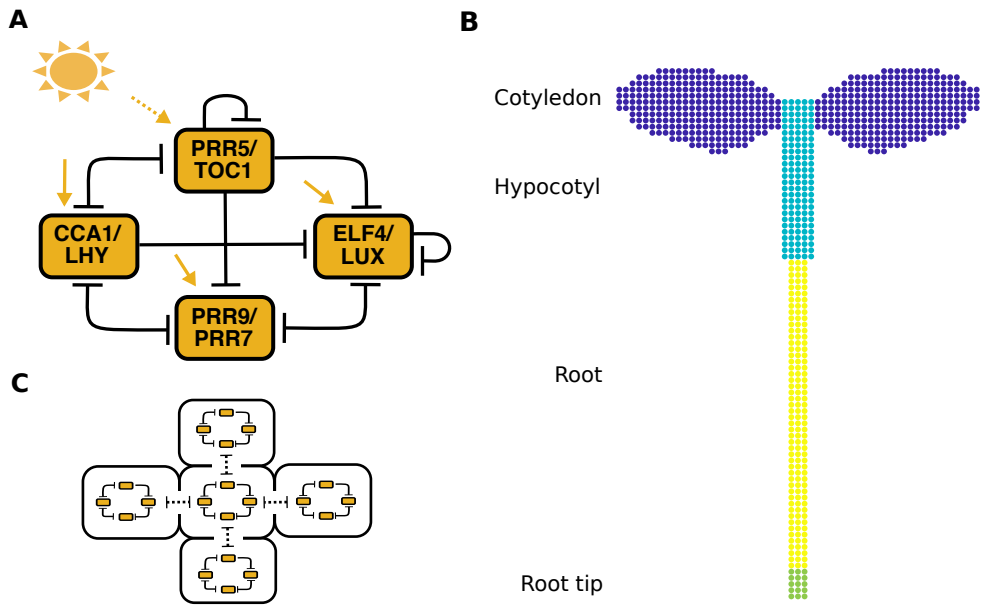

653

654 **Fig 1. The structure of the spatial circadian clock model.** (A) Summary of the modified
655 compact circadian clock model used for simulations. The original compact model [31] is
656 modified to include a repression interaction between CCA1/LHY and PRR5/TOC1. Light input is
657 received by all gene pairs, but affects their production and degradation rates to different
658 degrees. Yellow dashed arrows represent light input at the transcriptional level and solid yellow
659 arrows represent light input at both the transcriptional and post-transcription level. "T" arrows
660 represent repression. (B) The network was implemented within each cell on a simplified
661 template of a seedling, with cells classified as either cotyledon (blue), hypocotyl (turquoise), root
662 (yellow), or root tip cells (green). (C) The network in each individual cell is coupled to the
663 neighboring cells through the level of *CCA1*/*LHY*. *CCA1*, *CIRCADIAN CLOCK ASSOCIATED 1*;
664 *ELF4*, *EARLY FLOWERING 4*; *LHY*, *LATE ELONGATED HYPOCOTYL*; LL, constant light;
665 *LUC*, *LUCIFERASE*; *LUX*, *LUX ARRHYTHMO*; *PRR*, *PSEUDO-RESPONSE REGULATOR*;
666 *TOC1*, *TIMING OF CAB EXPRESSION 1*.

667

668

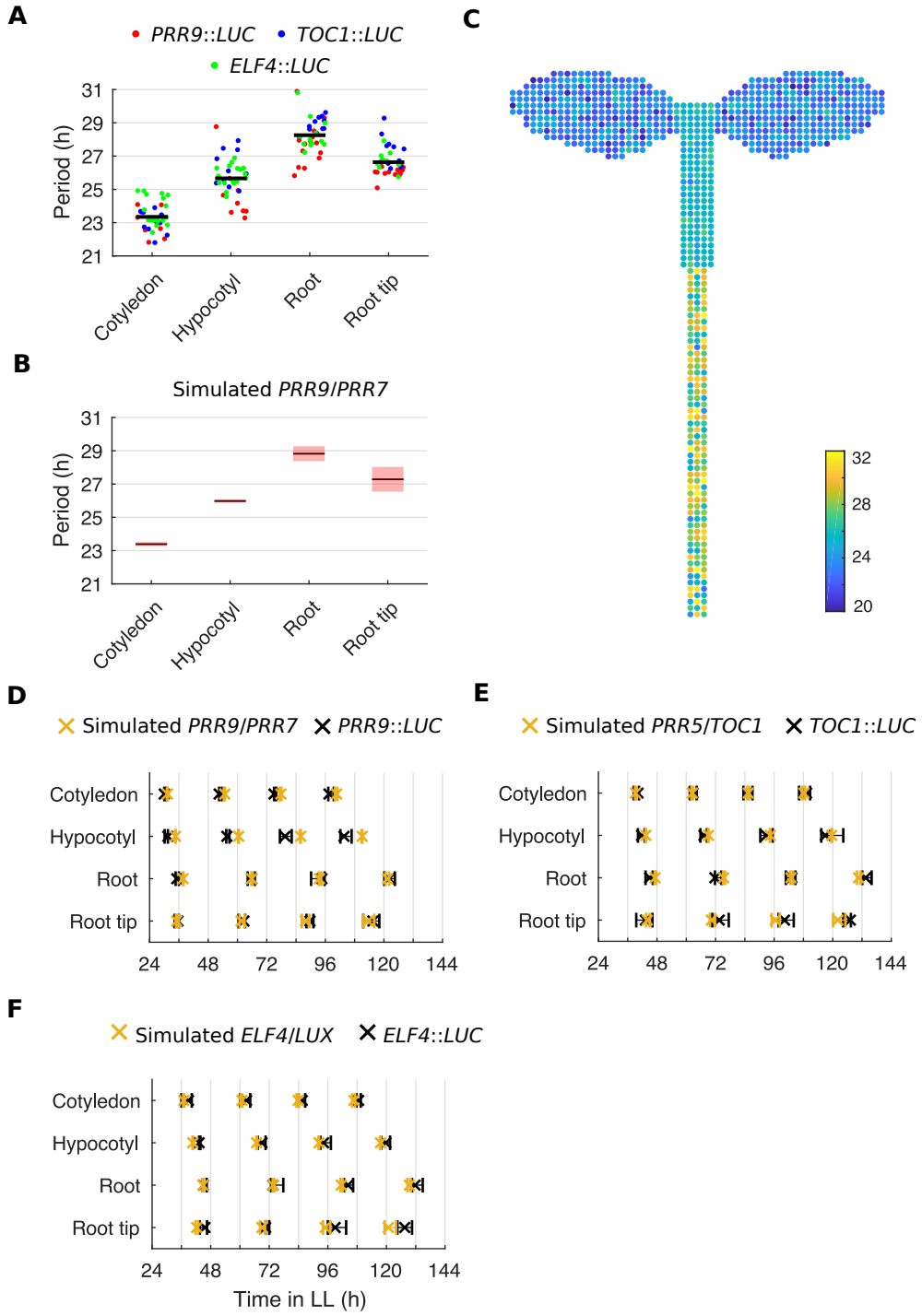

Fig 2. Regional differences in light input can generate the period structure observed experimentally. (A) Period estimates of *PRR9*::*LUC*, *TOC1*::*LUC*, and *ELF4*::*LUC* for different organs imaged under LL. Each data point represents a period estimate from the organ of a single seedling, made from time-lapse movies carried out previously [14]. The horizontal black

674 line shows the mean. (B) Period estimates of simulated *PRR9/PRR7* expression, measured
675 from regions within the template seedling. The black line indicates the mean and the red shaded
676 area one standard deviation of 18 independent simulations. (C) Periods of individual cells
677 plotted on the template seedling. The color of the cell represents the speed of the oscillation. By
678 assuming higher light input to the cells in the cotyledon, hypocotyl, and root tip, the model
679 approximates the period differences observed between regions in experiments, A. A noise
680 parameter was adjusted for each region to simulate the variability of periods observed in single
681 cell experiments (S1 Fig). (D−F) Times of peaks of simulated *PRR9*/*PRR7* and *PRR9*::*LUC* (D),
682 simulated *PRR5*/*TOC1* and *TOC1*::*LUC* (E), or simulated *ELF4*/*LUX* and *ELF4*::*LUC* (F), in
683 different organs under LL. Simulations include different levels of light input to regions and cell-
684 to-cell coupling (J = 2). Plots represent the 25th percentile, median, and the 75th percentile for
685 the peak times of oscillations scored as rhythmic, n = 9 simulations. *CCA1*, *CIRCADIAN CLOCK*
686 *ASSOCIATED 1*; CV, coefficient of variation; *ELF4*, *EARLY FLOWERING 4*; *LHY*, *LATE*
687 *ELONGATED HYPOCOTYL*; LL, constant light; *LUC*, *LUCIFERASE*; *LUX*, *LUX ARRHYTHMO*;
688 *PRR*, *PSEUDO-RESPONSE REGULATOR*; *TOC1*, *TIMING OF CAB EXPRESSION 1*.
689
690
691

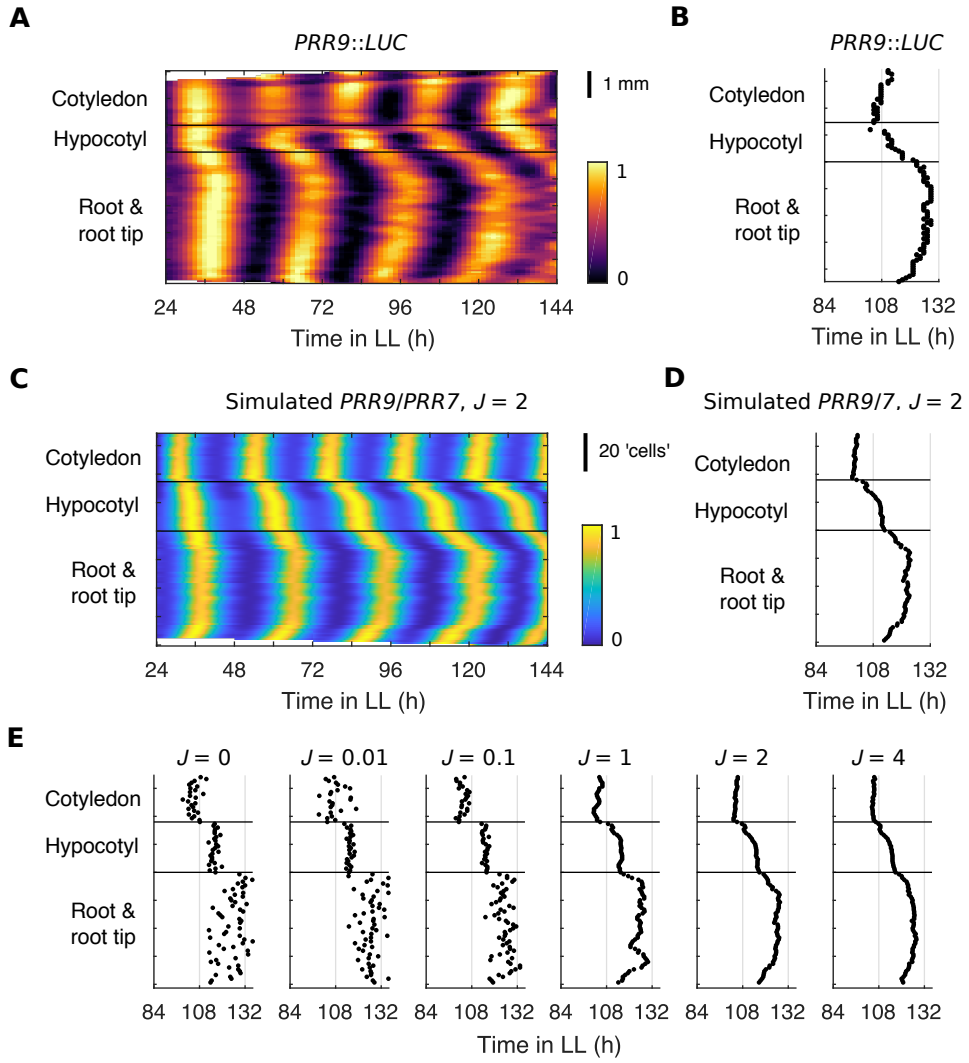

Fig 3. Local sharing of mRNA can reproduce experimentally observed spatial waves of clock gene expression. (A) Representative intensity plot of *PRR9*::*LUC* expression across longitudinal sections of a single seedling under LL. (B) Times of the final peaks of the *PRR9*::*LUC* intensity plot simulated under LL. (C) Representative intensity plot of simulated *PRR9*/*PRR7* expression across longitudinal sections of a single seedling under LL. Simulations include different levels of light input to regions and cell-to-cell coupling (J = 2). (D) Times of the final peaks of the simulated *PRR9*/*PRR7* intensity plot simulated under LL. (E) Times of the final peak of simulated *PRR9*/*PRR7* intensity plots, each simulated under LL with increasing strength of coupling, J. Experimental data is an analysis of time-lapse movies carried out previously [14].

702 *PRR*, *PSEUDO RESPONSE REGULATOR*; LL, constant light; *LUC*, *LUCIFERASE*. *TOC1,*

703 *TIMING OF CAB EXPRESSION 1.*

704

705

706

707

708

709

710

711

712

713

714

715

716

717

718

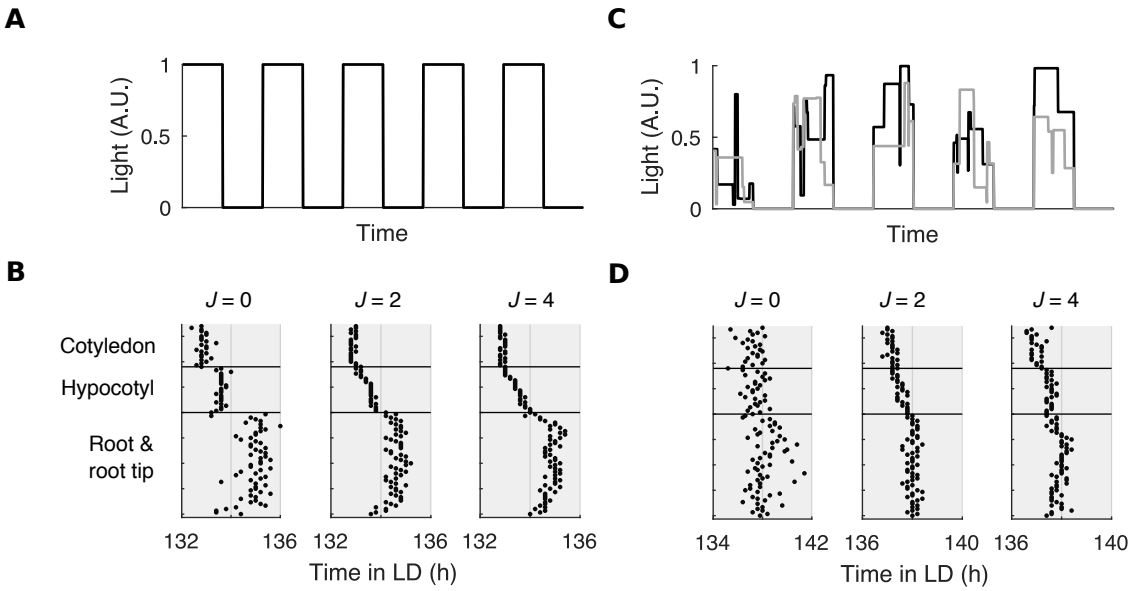

Fig 4. Regional phase differences persist under idealized and noisy LD cycles. (A) Schematic of idealized LD cycles, without fluctuations in light levels during the daytime. (B) Times of the final peak of simulated *PRR5*/*TOC1* intensity plots, each simulated under idealized LD with increasing strength of coupling, *J*. (C) Schematic of noisy LD cycles, with fluctuations in light levels during the daytime. Each line represents an LD cycle for a single cell. (D) Times of the final peak of simulated *PRR5*/*TOC1* intensity plots, each simulated under noisy LD with increasing strength of coupling, *J*. LD, light-dark; *PRR*, *PSEUDO-RESPONSE REGULATOR*; *TOC1*, *TIMING OF CAB EXPRESSION 1*.

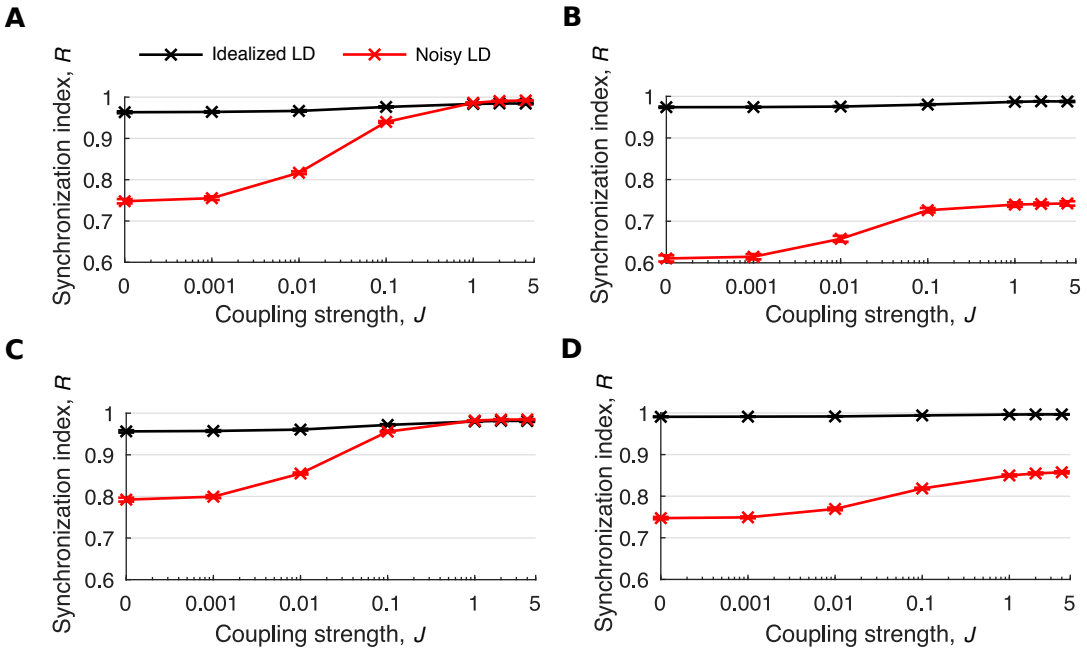

Fig 5. Cell-to-cell coupling maintains global synchrony under noisy LD cycles. (A–D) Quantification of phase coherence by the synchronization index, *R*, for simulated *CCA1*/*LHY* (A), *PRR9*/*PRR7* (B), *PRR5*/*TOC1* (C) or *ELF4*/*LUX* (D) mRNA expression under idealized or noisy LD cycles. Simulations included increasing strengths of coupling, *J*. Color legends are as in A. Data points represent the mean ± standard deviation, *n* = 9 simulations. *CCA1*, *CIRCADIAN CLOCK ASSOCIATED 1*; *ELF4*, *EARLY FLOWERING 4*; LD, light-dark; *LHY*, *LATE ELONGATED HYPOCOTYL*; *LUX*, *LUX ARRHYTHMO*; *LUC*, *LUCIFERASE*; *PRR*, *PSEUDO-RESPONSE REGULATOR*; *TOC1*, *TIMING OF CAB EXPRESSION 1*.

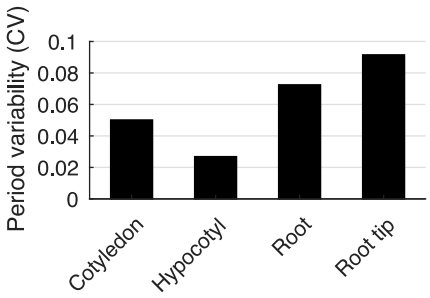

S1 Fig. Between-cell variability of CCA1-YFP rhythms. Between-cell variability of periods within different organs. The periods were estimated from single cell time-lapse movies of CCA1-YFP expression carried out previously [8]. *CCA1*, *CIRCADIAN CLOCK ASSOCIATED 1*; CV, coefficient of variation; YFP, yellow fluorescent protein.

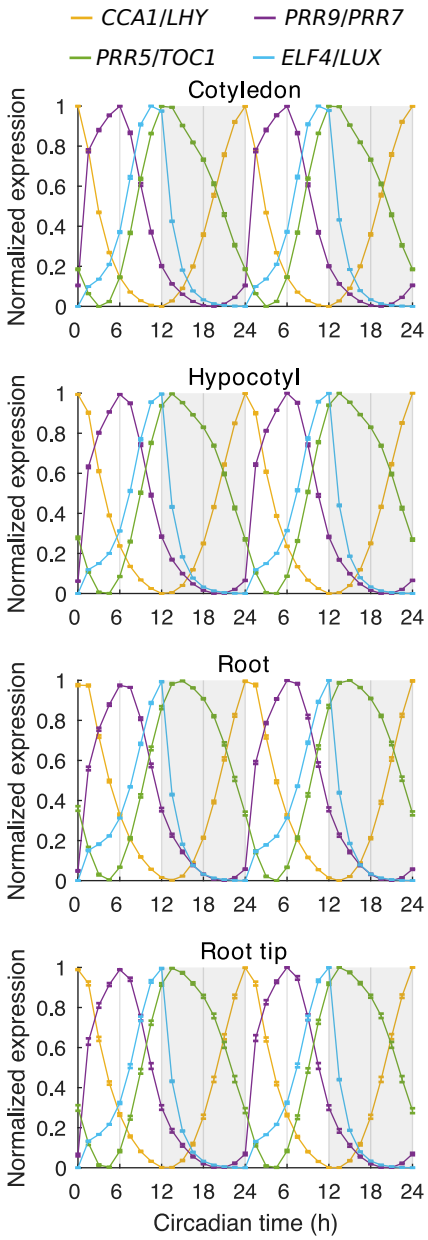

S2 Fig. Simulated expression of clock genes in different regions under LD cycles. Expression of simulated *CCA1*/*LHY*, *PRR9*/*PRR7*, *PRR5*/*TOC1*, and *ELF4*/*LUX* from regions of the seedling template 96–144 h after the beginning of LD cycles. The light input, *L*, was varied depending on whether the cell was within the cotyledon (*L* = 1.35), hypocotyl (*L* = 1.10), root (*L* = 0.90), or root tip (*L* = 1.03) region, and coupling was present between cells (*J* = 2). Data represent the mean ± standard error, *n* = 9 simulations. *CCA1*, *CIRCADIAN CLOCK ASSOCIATED 1*; *ELF4*, *EARLY FLOWERING 4*; LD, light-dark; *LHY*, *LATE ELONGATED*

760 *HYPOCOTYL; LUC*, *LUCIFERASE*; *LUX*, *LUX ARRHYTHMO*; *PRR*, *PSEUDO-RESPONSE*

761 *REGULATOR*; *TOC1*, *TIMING OF CAB EXPRESSION 1*.

762

763

764

765

766

767

768

769

770

771

772

773

774

775

776

777

778

779

780

781

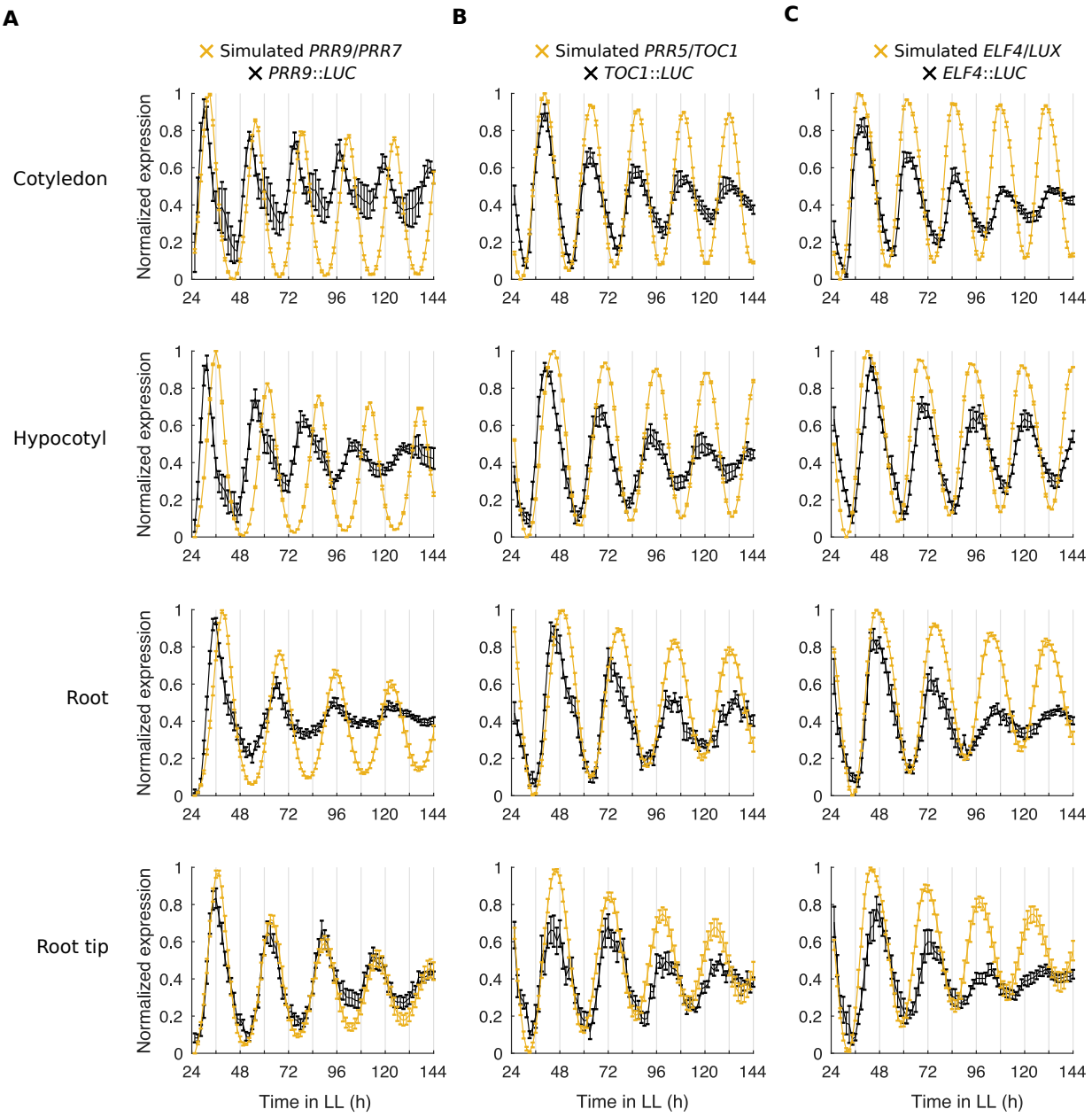

782

783 **S3 Fig. Simulated expression of multiple core clock genes under LL qualitatively match**

784 **luciferase reporter experiments.** (A–C) Expression of simulated *PRR9*/*PRR7* and *PRR9*::*LUC*

785 (A), simulated *PRR5*/*TOC1* and *TOC1*::*LUC (B)*, or simulated *ELF4*/*LUX* and *ELF4*::*LUC* (C) in

786 different organs under LL. Simulations include different levels of light input to regions and cell-

787 to-cell coupling (J = 2). Data represent the mean ± standard error of organs scored as rhythmic.

788 n = 9 simulations. Experimental data is from time-lapse movies carried out previously [14].

789 *ELF4*, *EARLY FLOWERING 4*; LL, constant light; *LUC*, *LUCIFERASE*; *LUX*, *LUX*
790 *ARRHYTHMO*; *PRR*, *PSEUDO-RESPONSE REGULATOR*; *TOC1*, *TIMING OF CAB*
791 *EXPRESSION 1*.
792
793
794
795
796
797
798
799
800
801
802
803
804
805
806
807
808
809
810
811
812

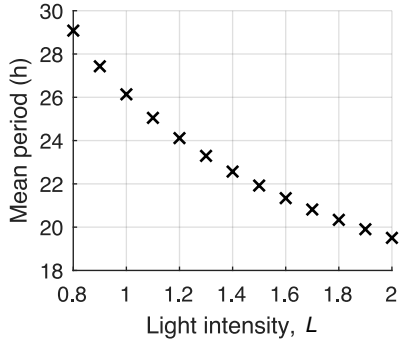

S4 Fig. Higher light intensities cause simulations to run faster. The mean peak-to-peak time of simulated *PRR9*/PRR7 expression with increasing intensities of light, *L*. A single instance of the model was implemented at each *L*, without cell-to-cell coupling or variation in gene expression. *L* values below 0.8 caused damping in the original and modified De Caluwe implementation. *PRR*, *PSEUDO-RESPONSE REGULATOR*.

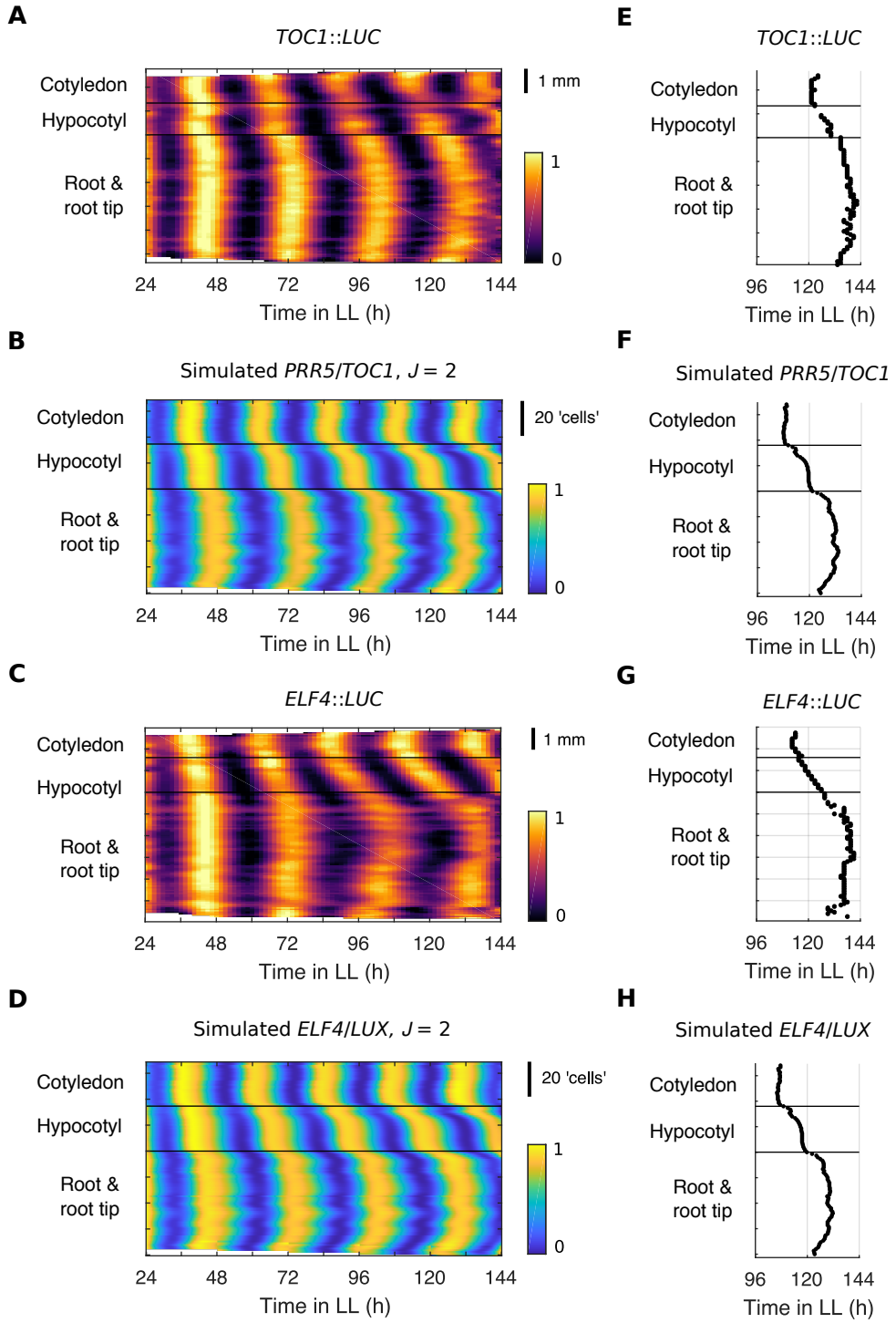

S5 Fig. Local sharing of mRNA can reproduce experimentally observed spatial waves of clock gene expression for multiple core clock genes. (A–D) Representative intensity plot of *TOC1*::*LUC* (A), simulated *PRR5*/*TOC1* (B), *ELF4*::*LUC* (C) and simulated *ELF4*/*LUX* (D) expression across longitudinal sections of a single seedling under LL. Simulations include

833 different levels of light input to regions and cell-to-cell coupling (J = 2). (E–H) Times of the final
834 peak of *TOC1*::*LUC* (E), simulated *PRR5*/*TOC1* (F), *ELF4*::*LUC* (G) and simulated *ELF4*/*LUX*
835 (H) intensity plots. Experimental data is an analysis of time-lapse movies carried out previously
836 [14]. *ELF4*, *EARLY FLOWERING 4*; *LHY*, *LATE ELONGATED HYPOCOTYL*; LL, constant light;
837 *LUX*, *LUX ARRHYTHMO*; *PRR5*, *PSEUDO-RESPONSE REGULATOR 5; TOC1*, *TIMING OF*
838 *CAB EXPRESSION 1*.
839
840
841
842
843
844
845
846
847
848
849
850
851
852
853
854

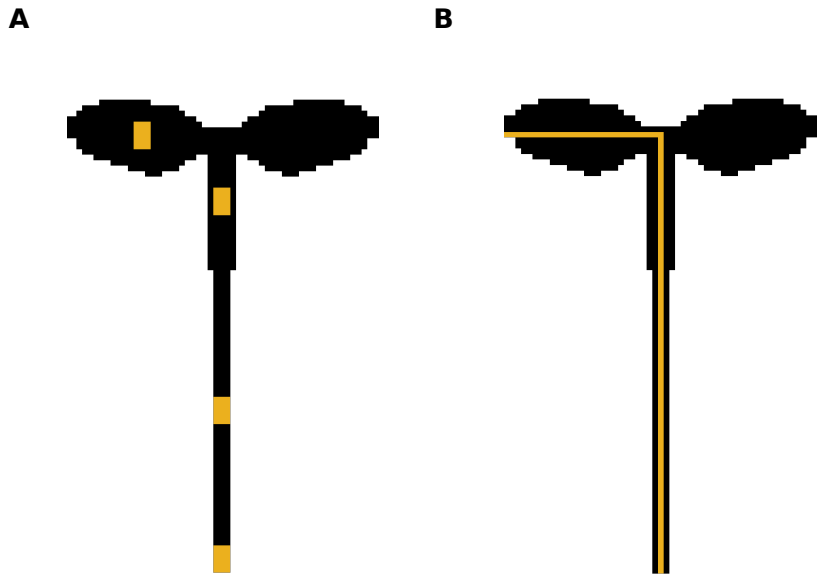

855

856 **S6 Fig. Spatial analysis of rhythms across the simplified template of a plant.** (A) To
857 measure the period and phase of an organ, the expression was extracted from 3-by-3 pixel
858 regions of interest (yellow squares). (B) To produce space-time plots of gene expression (e.g.
859 Fig 3A), the mean expression of sections perpendicular across the central axis (yellow line) of
860 the template were taken. Luciferase space-time plots were created similarly, as described
861 previously [14] (Methods).

862

863

864

865

866

867

868

869

870

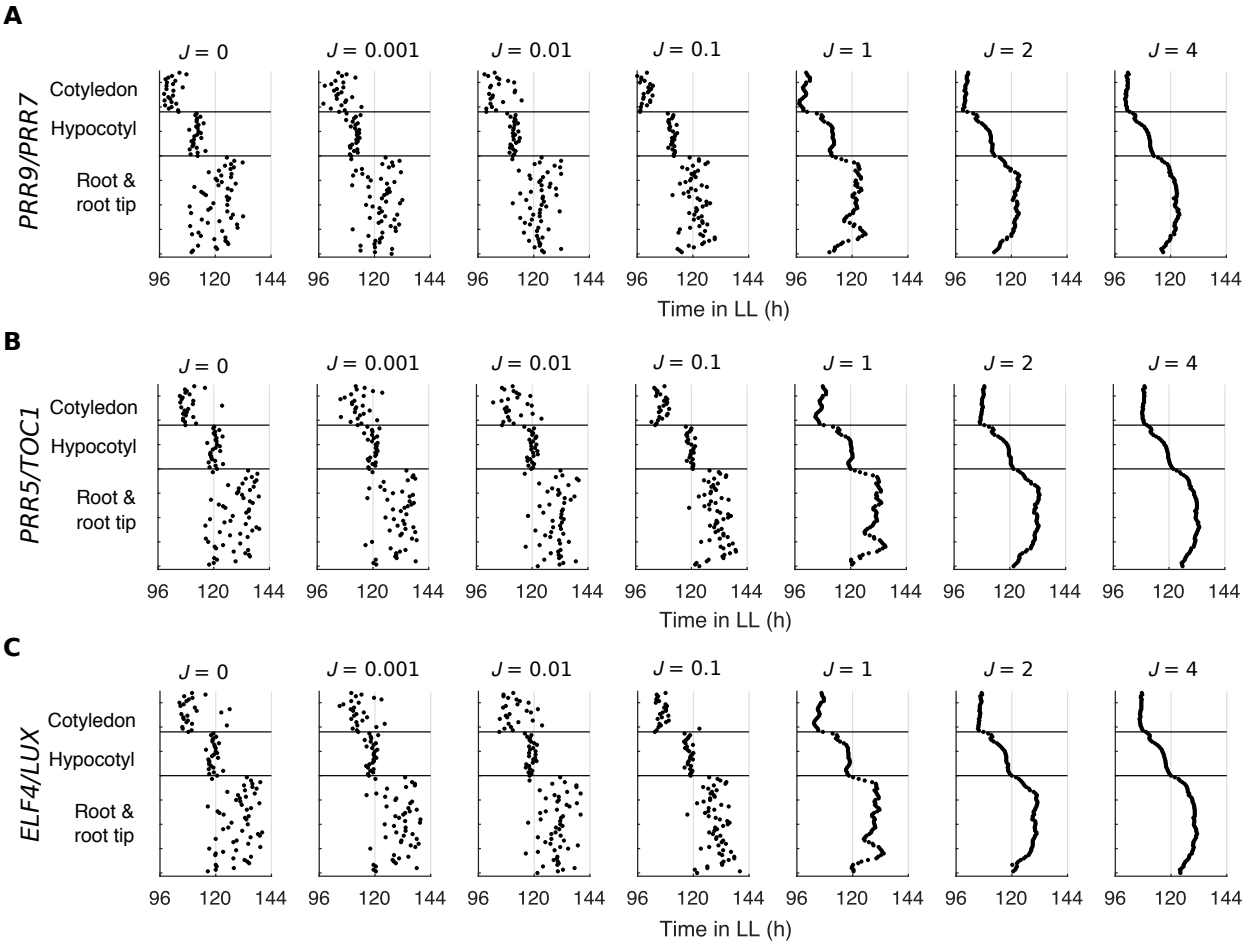

S7 Fig. Times of the final peaks of simulated expression under LL with increasing strengths of coupling. (A–C) Times of the final peak of simulated *PRR9/PRR7* (A), simulated *PRR5*/*TOC1* (B), and simulated *ELF4*/*LUX* (C) intensity plots, each simulated under LL with increasing strength of coupling, *J*. *ELF4*, *EARLY FLOWERING 4*; LL, constant light; *LUX*, *LUX ARRHYTHMO*; *PRR*, *PSEUDO-RESPONSE REGULATOR; TOC1*, *TIMING OF CAB EXPRESSION 1*.

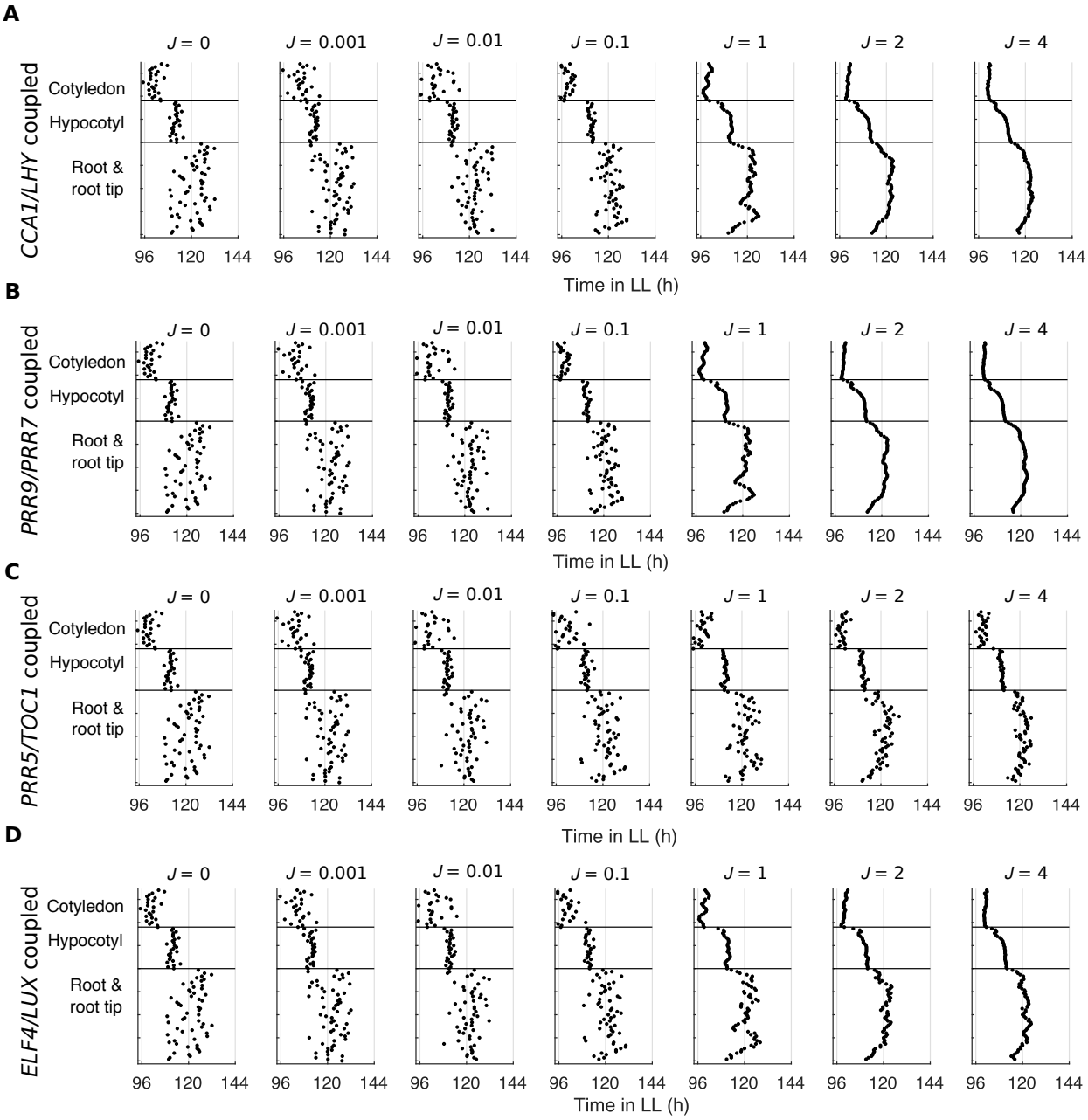

S8 Fig. Times of the final peaks of simulated expression under LL with the sharing of different clock gene mRNA between cells. (A–C) Times of the final peak of simulated *PRR9/PRR7* intensity plots, each simulated with the sharing of *CCA1*/*LHY*, *PRR9*/*PRR7*, *PRR5*/*TOC1*, or *ELF4*/*LUX* mRNA between neighbor cells. Simulations were under LL with increasing strength of coupling, *J*. *CCA1*, *CIRCADIAN CLOCK ASSOCIATED 1*; *ELF4*, *EARLY FLOWERING 4*; *LHY*, *LATE ELONGATED HYPOCOTYL*; LL, constant light; *LUX*, *LUX*

889 *ARRHYTHMO*; *PRR*, *PSEUDO-RESPONSE REGULATOR; TOC1*, *TIMING OF CAB*

890 *EXPRESSION 1*.

891

892

893

894

895

896

897

898

899

900

901

902

903

904

905

906

907

908

909

910

911

912

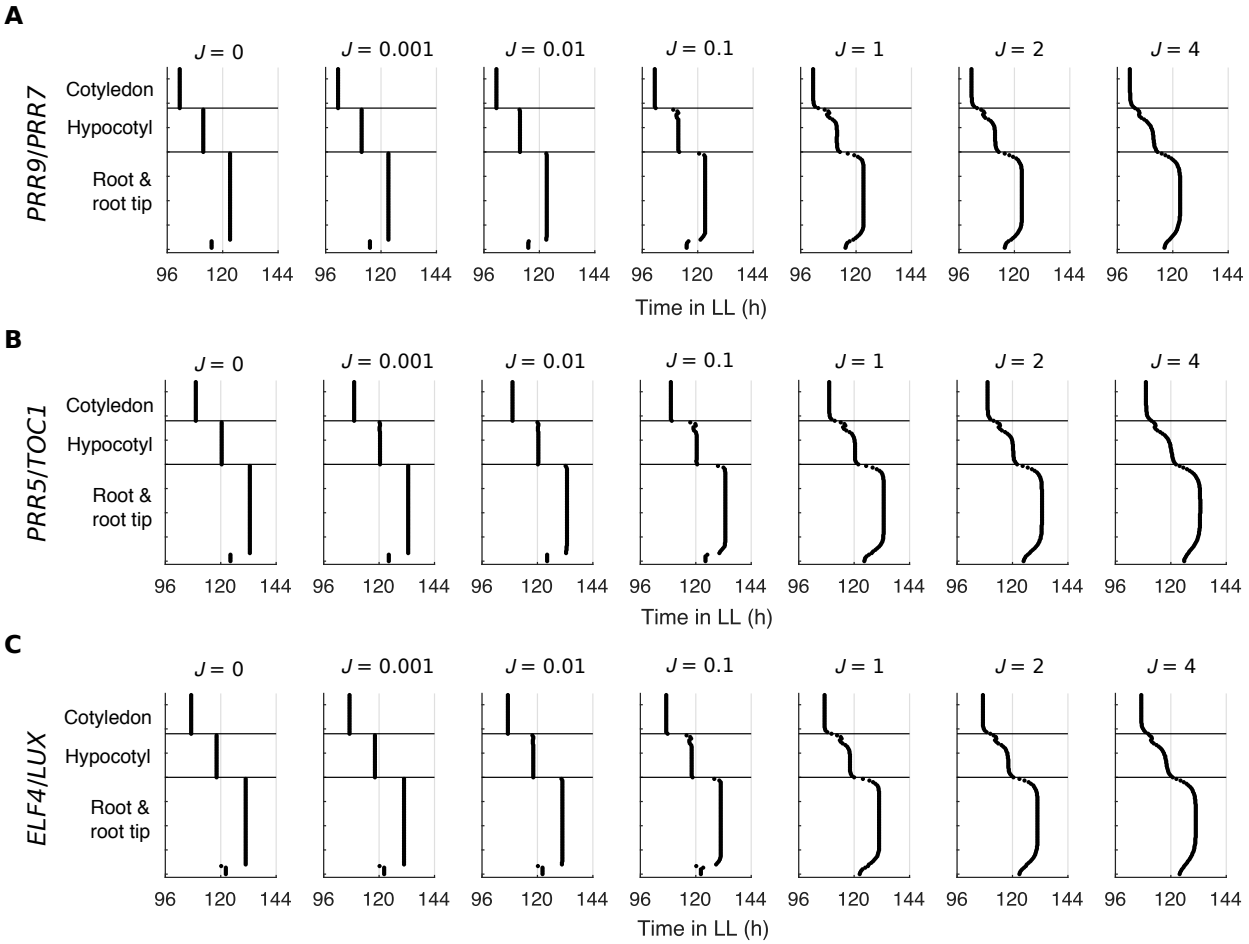

S9 Fig. Times of the final peaks of simulated expression under LL without variation in gene expression. (A–C) Times of the final peak of simulated *PRR9*/*PRR7* (A)*, PRR5*/*TOC1* (B), or *ELF4*/*LUX* (C) intensity plots, each simulated with the sharing of *CCA1*/*LHY* mRNA between 4 neighbor cells, but without cell-to-cell variation in gene expression. Simulations were under LL with increasing strength of coupling, *J*. *CCA1*, *CIRCADIAN CLOCK ASSOCIATED 1*; *ELF4*, *EARLY FLOWERING 4*; *LHY*, *LATE ELONGATED HYPOCOTYL*; LL, constant light; *LUX*, *LUX ARRHYTHMO*; *PRR*, *PSEUDO-RESPONSE REGULATOR; TOC1*, *TIMING OF CAB EXPRESSION 1*.

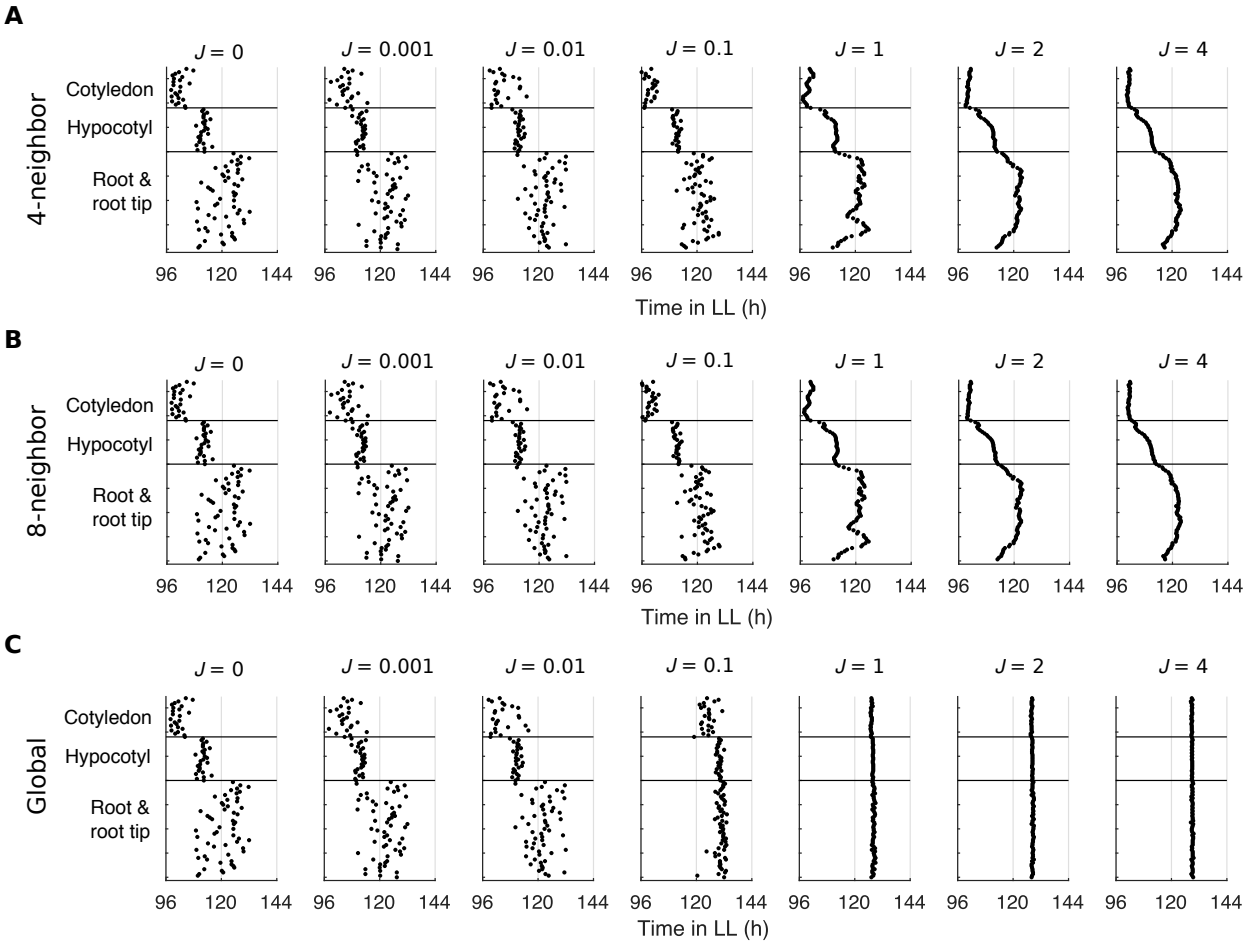

S10 Fig. Times of the final peaks of simulated expression under LL with different coupling rules. (A–C) Times of the final peak of simulated *PRR9/PRR7* intensity plots, each simulated under LL with the sharing of *CCA1*/*LHY* mRNA between the 4 nearest neighbor cells (A), 8 nearest neighbor cells (B), or globally (all-to-all) (C). Simulations were run under LL with increasing strength of coupling, *J*. *CCA1*, *CIRCADIAN CLOCK ASSOCIATED 1*; *LHY*, *LATE ELONGATED HYPOCOTYL*; LL, constant light; *PRR*, *PSEUDO-RESPONSE REGULATOR*.

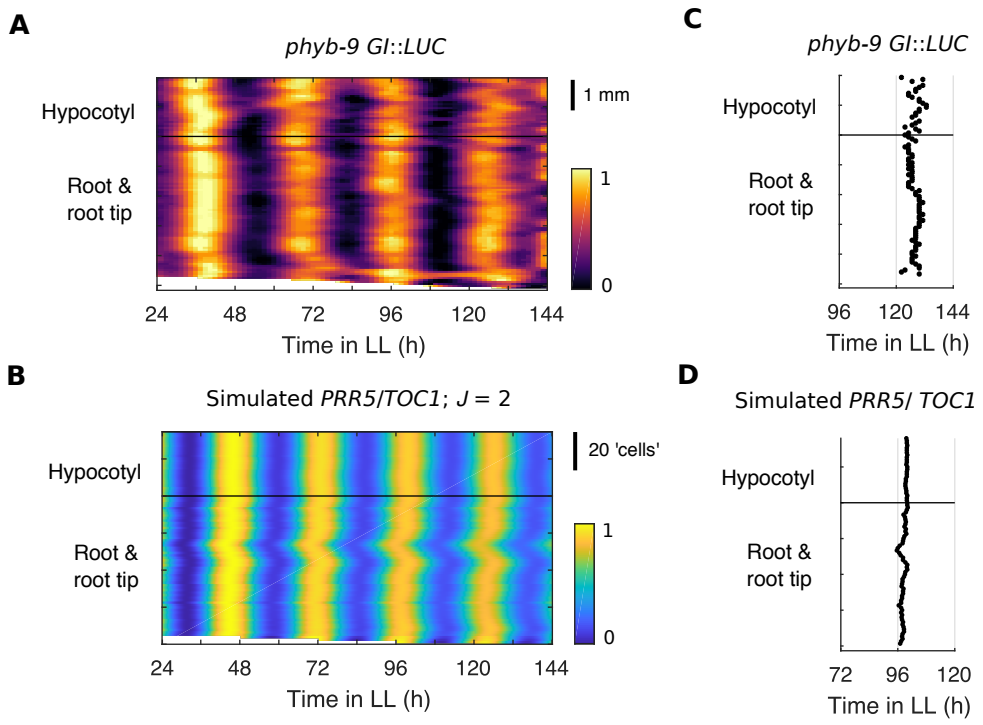

S11 Fig. Simulations with equal light input to regions predicts the loss of spatial waves observed in the *phyb-9* mutant. (A) Representative intensity plot of *GI*::*LUC* expression across longitudinal sections of a single seedling under constant red light. Imaging was performed in the light sensing mutant *phyb-9* background. (B) Representative intensity plot of simulated *PRR5*/*TOC1* expression across longitudinal sections of a single seedling under LL. Simulations were performed with equal low light to all regions (L = 0.85) and cell-to-cell coupling (J = 2). (C) Times of the final peaks of *phyb-9 TOC1*::*LUC* intensity plots. (D) Times of the final peaks of simulated *PRR5*/*TOC1* intensity plots, with equal low light to all regions (L = 0.85) and cell-to-cell coupling (J = 2). Experimental data is an analysis of time-lapse movies carried out previously [14]. Intensity plots are limited to the lower hypocotyl and root due to rapid elongation of the hypocotyl in the *phyb-9* mutant. *PRR*, *PSEUDO RESPONSE REGULATOR*; LL, constant light; *LUC*, *LUCIFERASE*. *TOC1, TIMING OF CAB EXPRESSION 1.*

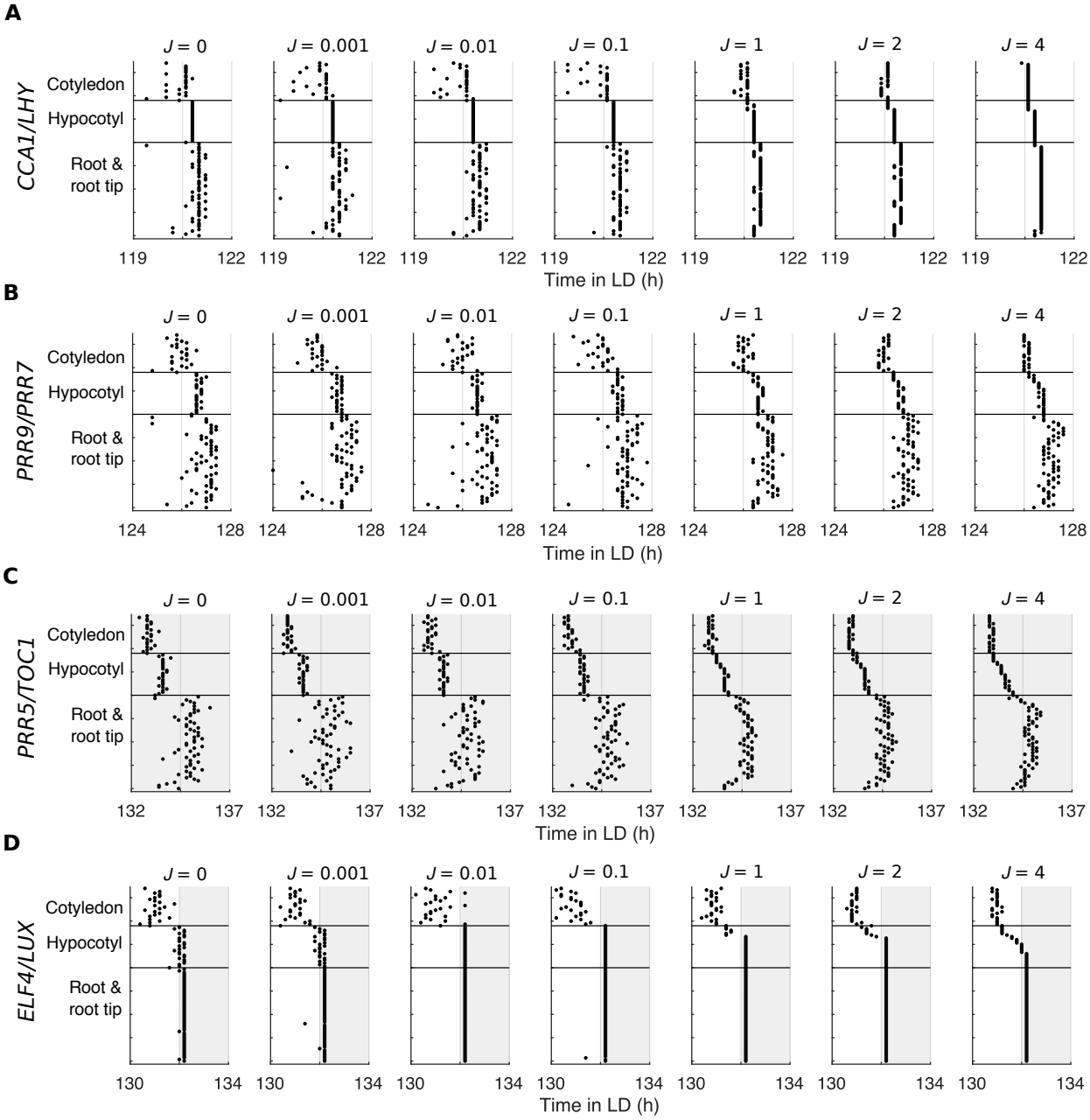

S12 Fig. Times of the final simulated peaks of expression under idealized LD cycles with increasing strengths of coupling. (A–D) Times of the final peak of simulated *CCA1*/*LHY* (A), *PRR9/PRR7* (B), *PRR5*/*TOC1* (C), and *ELF4*/*LUX* (D) intensity plots, each simulated under idealized LD cycles with increasing strength of coupling, *J*. Cells were exposed to idealized LD cycles during simulations. Grey background indicates nighttime. *ELF4* appears synchronized

955 when the peak coincides with the dark transition as darkness causes strong repression of *ELF4*
956 expression. *CCA1*, *CIRCADIAN CLOCK ASSOCIATED 1*; *ELF4*, *EARLY FLOWERING 4*; LD,
957 light-dark; *LHY*, *LATE ELONGATED HYPOCOTYL*; *LUX*, *LUX ARRHYTHMO*; *PRR*, *PSEUDO*
958 *RESPONSE REGULATOR*; *TOC1*, *TIMING OF CAB EXPRESSION 1*.
959
960
961
962
963
964
965
966
967
968
969
970
971
972
973
974
975
976

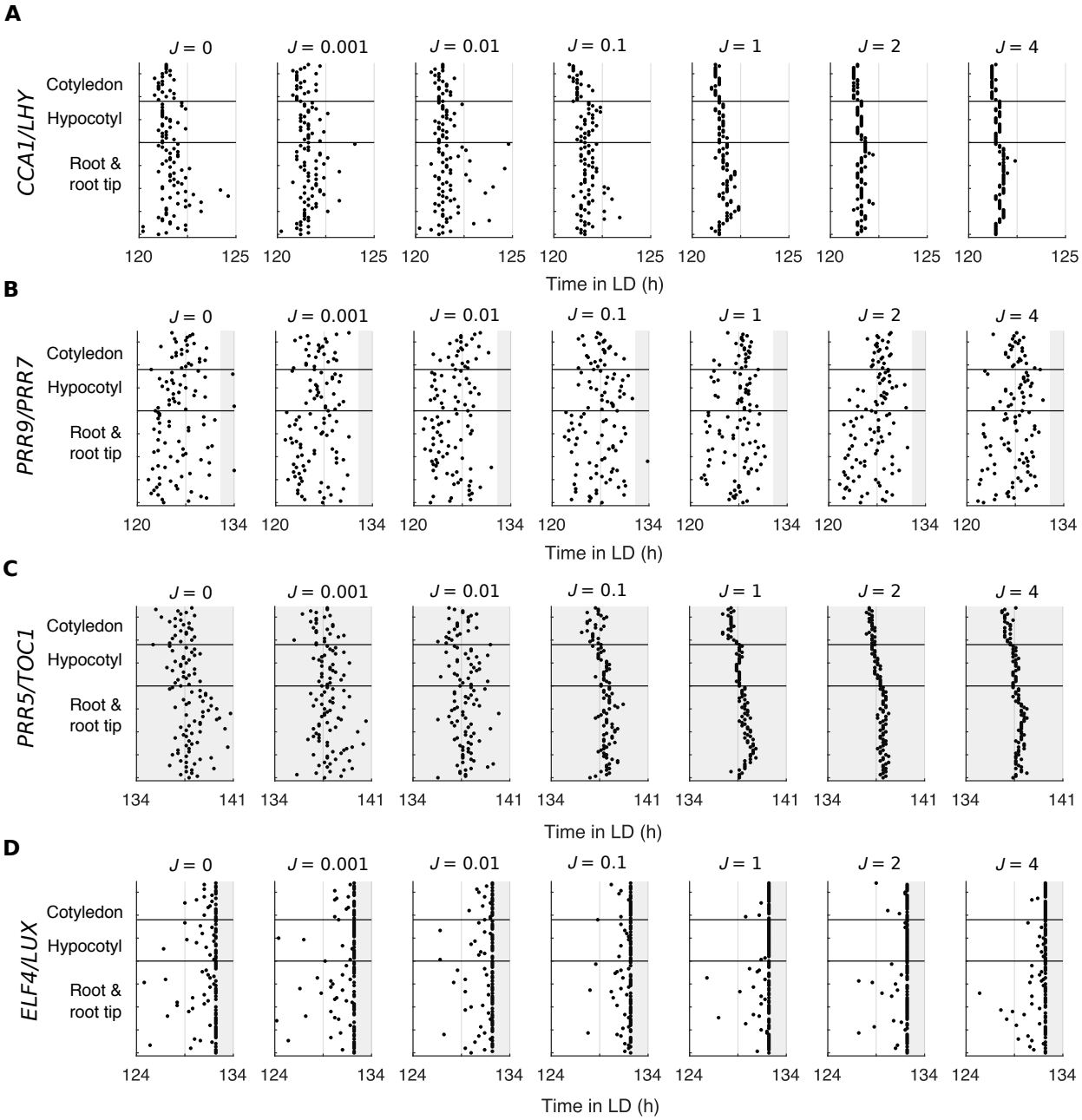

S13 Fig. Times of the final simulated peaks of expression under noisy LD cycles with increasing strengths of coupling. (A–D) Times of the final peak of simulated *CCA1*/*LHY* (A), *PRR9/PRR7* (B), simulated *PRR5*/*TOC1* (C), and simulated *ELF4*/*LUX* (D) intensity plots, each simulated under idealized LD cycles with increasing strength of coupling, *J*. Cells were exposed to idealized LD cycles during simulations. Grey background indicates nighttime. *ELF4* appears synchronized when the peak coincides with the dark transition as darkness causes strong

984 repression of *ELF4* expression. *CCA1*, *CIRCADIAN CLOCK ASSOCIATED 1*; *ELF4*, *EARLY*
985 *FLOWERING 4*; LD, light-dark; *LHY*, *LATE ELONGATED HYPOCOTYL*; *LUX*, *LUX*
986 *ARRHYTHMO*; *PRR*, *PSEUDO RESPONSE REGULATOR*; *TOC1*, *TIMING OF CAB*
987 *EXPRESSION 1*.
988
989
990
991
992
993
994
995
996
997
998
999
1000
1001
1002
1003
1004
1005
1006
1007

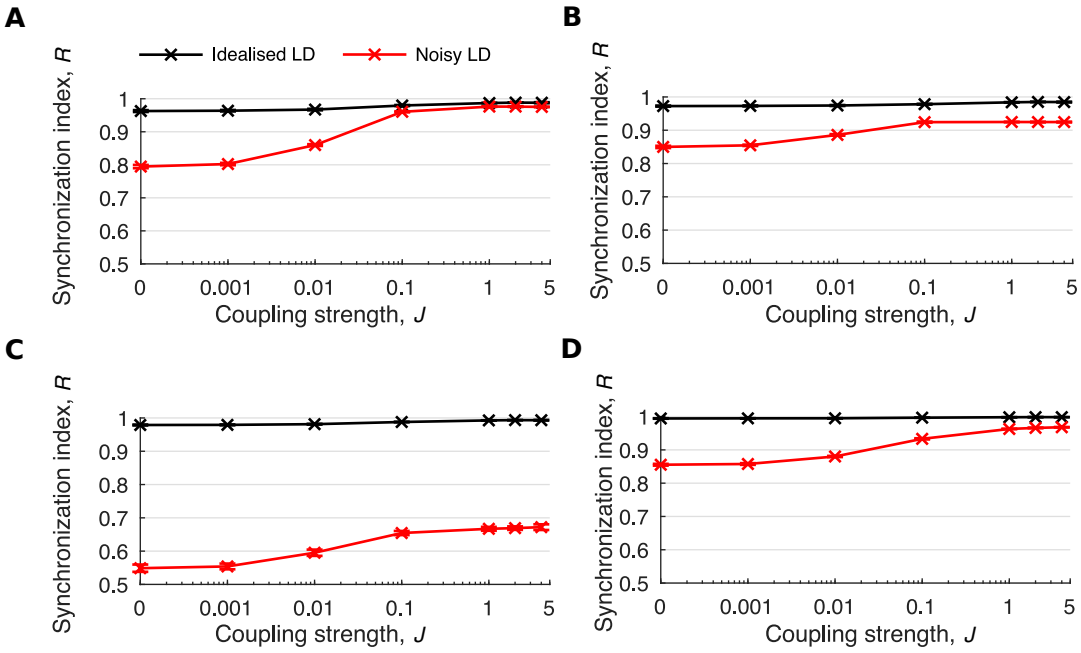

S14 Fig. Cell-to-cell coupling increases the synchrony of protein oscillations under realistic LD cycles. (A–D) Quantification of phase coherence by the synchronization index, *R*, for simulated *CCA1*/*LHY* (A), *PRR9*/*PRR7* (B), *PRR5*/*TOC1* (C) or *ELF4*/*LUX* (D) protein expression under idealized or noisy LD cycles. Simulations included increasing strengths of coupling, *J*. Color legends are as in A. Data points represent the mean ± standard deviation, *n* = 9 simulations. CCA1, CIRCADIAN CLOCK ASSOCIATED 1; ELF4, EARLY FLOWERING 4; LD, light-dark; LHY, LATE ELONGATED HYPOCOTYL; LUX, LUX ARRHYTHMO; PRR, PSEUDO RESPONSE REGULATOR; TOC1, TIMING OF CAB EXPRESSION 1.

1024 **S1 Table. Parameter values for the spatial clock model.**

Parameter	Description	Original value [31]	Re-optimized value
v_1	*CCA1*/*LHY* synthesis	4.6 nM h^{-1}	4.58 nM h^{-1}
v_{1L}	*CCA1*/*LHY* light-induced synthesis	3.0 nM h^{-1}	3.0 nM h^{-1}
v_{2A}	*PRR9*/*PRR7* synthesis	1.3 nM h^{-1}	1.27 nM h^{-1}
v_{2L}	*PRR9*/*PRR7* light-induced synthesis	5.0 nM h^{-1}	5.0 nM h^{-1}
v_3	*PRR5*/*TOC1* synthesis	1.0 nM h^{-1}	1.0 nM h^{-1}
v_4	*ELF4*/*LUX* synthesis	1.5 nM h^{-1}	1.47 nM h^{-1}
k_{1L}	*CCA1*/*LHY* mRNA degradation (light)	0.53 h^{-1}	0.53 h^{-1}
k_{1D}	*CCA1*/*LHY* mRNA degradation (dark)	0.21 h^{-1}	0.21 h^{-1}
k_2	*PRR9*/*PRR7* mRNA degradation	0.35 h^{-1}	0.35 h^{-1}
k_3	*PRR5*/*TOC1* mRNA degradation	0.56 h^{-1}	0.56 h^{-1}
k_4	*ELF4*/*LUX* mRNA degradation	0.57 h^{-1}	0.57 h^{-1}
p_1	CCA1/LHY translation	0.76 h^{-1}	0.76 h^{-1}
p_{1L}	CCA1/LHY light-induced translation	0.42 h^{-1}	0.42 h^{-1}
p_2	PRR9/*PRR7* translation	1.0 h^{-1}	1.01 h^{-1}
p_3	PRR5/TOC1 translation	0.64 h^{-1}	0.64 h^{-1}
p_4	ELF4/LUX translation	1.0 h^{-1}	1.01 h^{-1}
d_1	CCA1/LHY degradation	0.68 h^{-1}	0.68 h^{-1}
d_{2D}	PRR9/*PRR7* degradation (dark)	0.51 h^{-1}	0.5 h^{-1}
d_{2L}	PRR9/*PRR7* degradation (light)	0.30 h^{-1}	0.29 h^{-1}
d_{3D}	PRR5/TOC1 degradation (dark)	0.48 h^{-1}	0.48 h^{-1}
d_{3L}	PRR5/TOC1 degradation (light)	0.78 h^{-1}	0.78 h^{-1}
d_{4D}	ELF4/LUX degradation (dark)	1.2 h^{-1}	1.21 h^{-1}
d_{4L}	ELF4/LUX degradation (light)	0.38 h^{-1}	0.38 h^{-1}
K_0	Inhibition of CCA1/LHY by CCA1/LHY	n/a	5.07 nM
K_1	Inhibition of CCA1/LHY by PRR9/PRR7	0.16 nM	0.16 nM
K_2	Inhibition of CCA1/LHY by PRR5/TOC1	1.2 nM	1.18 nM
K_4	Inhibition of PRR9/PRR7 by PRR5/TOC1	0.23 nM	0.40 nM
K_5	Inhibition of PRR9/PRR7 by ELF4/LUX	0.30	0.62 nM
K_{5b}	Inhibition of PRR9/PRR7 by CCA1/LHY	n/a	1.2 nM
K_6	Inhibition of PRR5/TOC1 by CCA1/LHY	0.46	0.46 nM
K_7	Inhibition of PRR5/TOC1 by PRR5/TOC1	2.0	2.0 nM
K_8	Inhibition of ELF4/LUX by CCA1/LHY	0.36	0.36 nM
K_9	Inhibition of ELF4/LUX by PRR5/TOC1	1.9	1.9 nM
K_{10}	Inhibition of ELF4/LUX by ELF4/LUX	1.9	1.9 nM

1025 *CCA1*, *CIRCADIAN CLOCK ASSOCIATED 1*; *ELF4*, *EARLY FLOWERING 4*; *LHY*, *LATE*
1026 *ELONGATED HYPOCOTYL*; *LUX*, *LUX ARRHYTHMO*; *PRR*, *PSEUDO-RESPONSE*
1027 *REGULATOR*; *TOC1*, *TIMING OF CAB EXPRESSION 1*.

1028 **S1 Video. Time-lapse of simulated *PRR9*/*PRR7* expression under LL.** Representative
1029 simulation of simulated *PRR9*/*PRR7* expression from individual cells of the plant template 24–
1030 144 h after transfer to LL. LL, constant light; *PRR*, *PSEUDO RESPONSE REGULATOR.*
1031
1032 **S2 Video. Time-lapse of *PRR9*::*LUC* expression under LL.** *PRR9*::*LUC* expression from a
1033 single representative seedling 24–144 h after transfer to LL. LL, constant light; *PRR9*, *PSEUDO*
1034 *RESPONSE REGULATOR9.*